Interference Purcell Filter for Fast, Modular, and Hardware-Efficient Quantum Measurement

by

Alec Yen

B.S. University of Tennessee, Knoxville (2020)

Submitted to the Department of Electrical Engineering and Computer Science
in partial fulfillment of the requirements for the degree of

Master of Science

at the

MASSACHUSETTS INSTITUTE OF TECHNOLOGY

September 2022

Author .....
Department of Electrical Engineering and Computer Science
August 26, 2022

Certified by .....
Kevin O'Brien
Assistant Professor of Electrical Engineering and Computer Science
Thesis Supervisor

Accepted by .....
Leslie A. Kolodziejski
Professor of Electrical Engineering and Computer Science
Chair, Department Committee on Graduate Students

Interference Purcell Filter for Fast, Modular, and Hardware-Efficient Quantum Measurement

by

Alec Yen

Submitted to the Department of Electrical Engineering and Computer Science
on August 26, 2022, in partial fulfillment of the
requirements for the degree of
Master of Science

Abstract

This thesis proposes a method to suppress Purcell decay for fast, modular, and hardware-efficient quantum measurement that we call an "interference" Purcell filter. Superconducting qubits experience many decay channels, one of which is Purcell decay, or leakage of the qubit state into the readout line. The proposed work suppresses Purcell decay by coupling the readout resonator at two points on the readout line to create a destructive interference effect, enabling a small and space-efficient footprint. The Purcell suppression is compatible with large resonator decay rates, making it a suitable design as quantum error correction schemes move toward faster readout. Unlike many existing methods to suppress Purcell decay, the proposed design does not require an "open" or weakly-coupled port, the removal of which would improve modularity and expedite the design of many-qubit systems.

Thesis Supervisor: Kevin O'Brien
Title: Assistant Professor of Electrical Engineering and Computer Science

Acknowledgments

I'd first like to thank my research advisor, Prof. Kevin O'Brien, for his guidance and for consistently going above and beyond as a mentor. His vision, insight, and excitement have inspired and shaped how I approach research problems; I thank him for the opportunity to work in this exciting field.

I'd also like to thank my labmates in the Quantum Coherent Electronics group: Kaidong, Bright, Greg, and Jenn for their camaraderie, both in and outside the lab. I thank them for their support and insightful discussions.

I'd like to acknowledge Prof. Ruonan Han for his gracious mentorship early in my graduate research. I'd also like to acknowledge my academic advisor Prof. Dave Perreault for his advice in navigating graduate school and classes.

Finally, I'd like to thank my parents for their constant love and support and for always enabling me to achieve my dreams. Their example is a constant standard for me in all things.

Contents

List of Figures

List of Tables

Chapter 1

Introduction

The promise of quantum computing has captivated many as a revolutionary paradigm for computation. Using superposition and entanglement, concepts foreign to classical computing, quantum algorithms enable accurate simulation of large quantum systems. This capability would transform medicine and chemistry [1], such as drug and battery research, and accelerate algorithms for optimization [2], factoring [3], and machine learning [4].

Superconducting quantum circuits have emerged as one of the most promising platforms for quantum computers [5, 6]. Using the nonlinearity of the Josephson junction, an addressable two-level system (or qubit) can be created. These man-made qubits are often referred to as artificial atoms and offer a much higher degree of engineering tunability than naturally-occurring atoms. Superconducting quantum computers have made strides toward quantum error correction and the implementation of logical qubits [7–9].

An essential feature for any quantum computer is the high-fidelity single-shot readout of multiple qubits. Standard readout techniques exploit the dispersive shift, a qubit-state-dependent frequency shift imposed on a coupled resonator by the qubit [10, 11]. Quantum-limited amplification [12–14] has allowed for single-shot measurements rather than averaging to determine the qubit state. The introduction of broadband parametric amplifiers [15, 16] has enabled the simultaneous measurement of multiple qubits. To improve the fidelity of qubit state measurement, Purcell filters

were introduced to enable faster readout while suppressing qubit damping via the Purcell effect [17–19].

A Purcell filter can consist of a bandpass filter resonator placed in series between the readout resonator and readout bus [20]. However, there is a premium on chip area, especially as the number of qubits on a single quantum chip grows. It is thus important to develop hardware-efficient approaches for Purcell suppression that save space and use existing components in the design. A common approach uses a transmission line resonator to double as both the readout bus and bandpass Purcell filter [18]. More recent work has also investigated careful positioning of the output coupling line to minimize decay of the dressed qubit mode [21]. However, these methods require an impedance mismatch ("open", weakly-coupled port, etc.) and a specific distance from the mismatch, which creates scaling and modularity challenges for quantum computers, as we will see in Ch. 3. In this thesis, we present a hardware-efficient Purcell filter that does not rely on such impedance mismatch and thus will be compatible with a more scalable and modular form of quantum measurement that we describe in Sec. 3.4.

1.1 Thesis Overview

This thesis proposal is organized as follows.

In Ch. 2, the relevant background of circuit quantum electrodynamics is discussed. The fundamentals of the quantum LC resonator and coupled LC resonators are presented. Next, a brief background on superconductivity and the Josephson junction is given. The superconducting qubit is then introduced, as well as a semiclassical method of black box quantization for analyzing weakly anharmonic superconducting circuits. Dispersive readout, the leading form of quantum nondemolition measurement, is then described. Reflection and transmission readout are explored using a coupled mode theory formulation. Sources of decoherence and noise, such as Purcell decay, are described, and the state-of-the-art methods for Purcell suppression are reviewed.

In Ch. 3, the limitations of current forms of qubit readout are discussed. The looming scaling challenges of massive, bulky, and high-magnetic field devices such as isolators and circulators are presented. Next, the modularity (or lack thereof) of quantum chips is discussed. We also discuss the limitations of bandpass Purcell filters as we move toward faster readout. Finally, we illustrate how this work fits into the larger picture of our proposal and ongoing work for more scalable and modular quantum measurement.

In Ch. 4, the proposed Purcell filter is described. First, we discuss the underlying principles and operation of the Purcell filter. Next, the Purcell suppression is modeled with classical SPICE simulation to determine the optimal design parameters and estimate Purcell suppression performance. The filter is then modeled with circuit quantization to simulate the qubit lifetime. An approximate circuit model is derived for compatibility with circuit quantization software. Performance is compared with and without the filter. Lastly, the physical layout of the filter, simulated qubit lifetime, and scattering parameters are presented.

Chapter 2

Superconducting Circuits

In this chapter, we review the relevant background of superconducting circuits.

2.1 The Quantum LC Resonator

We first review the fully quantum mechanical model for the LC oscillator, shown in Fig. 2-1. As we will show following a derivation similar to [22], this system is exactly analogous to a simple harmonic oscillator (SHO) taught in an introductory quantum mechanics class.

Since Josephson junctions are nonlinear with flux ϕ, we will find it is easiest to work with ϕ as the natural position coordinate and charge Q as the momentum. Since voltage is the derivative of flux, the flux and charge are related by $Q = C\dot{\phi}$, where C is the capacitance.

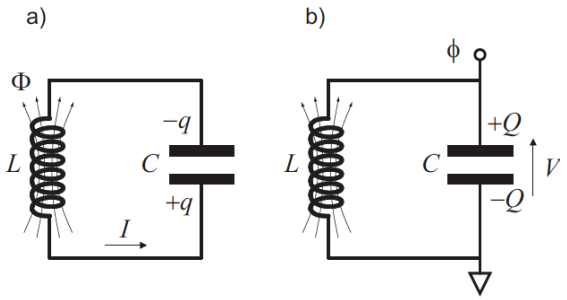

Figure 2-1: (a) Position coordinate of mass is taken to be q. (b) Position coordinate is taken to be ϕ. Figure from [22].

The Lagrangian is given by

$$\mathcal{L} = \frac{1}{2}C\dot{\phi}^2 - \frac{1}{2L}\phi^2. \tag{2.1}$$

The momentum conjugate to the flux is thus

$$Q = \frac{\delta\mathcal{L}}{\delta\dot{\phi}} = C\dot{\phi} \tag{2.2}$$

where the canonical commutation relation is given by

$$[\hat{Q}, \hat{\phi}] = -i\hbar. \tag{2.3}$$

We find the Hamiltonian to be

$$H = Q\dot{\phi} - \mathcal{L} = \frac{1}{2C}Q^2 + \frac{\phi^2}{2L} \tag{2.4}$$

with the voltage and current given by Hamilton's equations.

$$\dot{\phi} = +\frac{\partial H}{\partial Q} = +\frac{Q}{C} \tag{2.5}$$

$$\dot{Q} = -\frac{\partial H}{\partial \phi} = -\frac{\phi}{L} \tag{2.6}$$

This allows us to rewrite the Hamiltonian as

$$H = \frac{\hbar\Omega}{2}\left\{\hat{a}^\dagger\hat{a} + \hat{a}\hat{a}^\dagger\right\} = \hbar\Omega\left\{\hat{a}^\dagger\hat{a} + \frac{1}{2}\right\} \tag{2.7}$$

where the raising and lowering operators obey the relation $[\hat{a}, \hat{a}^\dagger]$ and are given by

$$\hat{a} = +i\frac{1}{\sqrt{2C\hbar\Omega}}\hat{Q} + \frac{1}{\sqrt{2L\hbar\Omega}}\hat{\phi} \tag{2.8}$$

$$\hat{a}^\dagger = -i\frac{1}{\sqrt{2C\hbar\Omega}}\hat{Q} + \frac{1}{\sqrt{2L\hbar\Omega}}\hat{\phi} \tag{2.9}$$

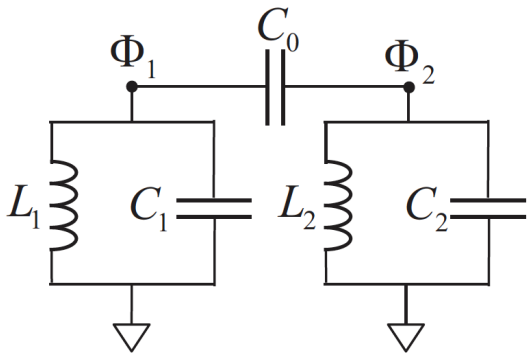

Figure 2-2: Coupled LC oscillators. Figure from [22].

It will be useful to re-express the charge and flux operators in terms of $\hat{a}$ and $\hat{a}^\dagger$

$$\hat{Q} = -iQ_{\text{ZPF}}\left(\hat{a} - \hat{a}^\dagger\right) \tag{2.10}$$

$$\hat{\phi} = \Phi_{\text{ZPF}}\left(\hat{a} + \hat{a}^\dagger\right) \tag{2.11}$$

where the zero-point fluctuations for charge and flux are given by

$$Q_{\text{ZPF}} = \sqrt{\frac{C\hbar\Omega}{2}} = \sqrt{\frac{\hbar}{2Z}} \tag{2.12}$$

$$\Phi_{\text{ZPF}} = \sqrt{\frac{L\hbar\Omega}{2}} = \sqrt{\frac{\hbar Z}{2}} \tag{2.13}$$

where Z is the characteristic impedance of the oscillator, given by

$$Z = \sqrt{\frac{L}{C}} \tag{2.14}$$

Note, that this choice of basis reflects that of Fig. 2-1b, though we could also have used the charge q as the position coordinate as in Fig. 2-1a. Also, note that the zero-point fluctuations obey the typical uncertainty product

$$Q_{\text{ZPF}}\Phi_{\text{ZPF}} = \frac{\hbar}{2} \tag{2.15}$$

It will be fruitful to find a Hamiltonian for two capacitively coupled LC resonators (see Fig. 2-2), as we will see in Sec. 2.5 is a good approximation for coupling between

a transmon qubit and a resonator. Two capacitive coupled resonators can be modeled by a Hamiltonian $H = H_0 + V$ where [22]

$$H_0 = \sum_{j=1}^{2} \hbar\omega_j \left(\hat{a}_j^\dagger \hat{a}_j + \frac{1}{2}\right) \tag{2.16}$$

$$V = -\beta\hbar\sqrt{\omega_1\omega_2}\left(\hat{a}_1 - \hat{a}_1^\dagger\right)\left(\hat{a}_2 - \hat{a}_2^\dagger\right) \tag{2.17}$$

where

$$\beta = \frac{C_0}{\sqrt{(C_1 + C_0)(C_2 + C_0)}} \tag{2.18}$$

2.2 Superconductivity and the Josephson Junction

To engineer a qubit, we must have an addressable two-level quantum system. To be addressable, the system must have some nonlinearity, in which the eigenenergies are anharmonic. The Josephson junction provides this nonlinearity. To understand how the Josephson junction enters this picture, we first give a background on superconductivity.

The discovery of superconductivity, a state where current flows without resistance, has unveiled a wide array of interesting physical phenomena. In this state, electrons travel in pairs, called Cooper pairs, due to an attractive phonon-mediated force [22]. These Cooper pairs can be broken apart by a finite excitation gap energy 2Δ. Once broken apart, they form an excited state.

In the limit of low temperatures and frequencies (where $k_B T, \hbar\omega << 2\Delta$), a macroscopic ground state can exist, reducing all other degrees of freedom in the enormous Hilbert space. In this manner, a macroscopic quantum system with one energy level has been created.

To create an excited state, consider two superconductors separated by a non-superconducting layer. An energy of 2Δ separates the ground state from densely packed excited states, which is usually approximated as a continuum. Unlike a non-superconducting junction, this tunneling process is coherent and characterizes how

Cooper pairs are exchanged. The voltage and current across this junction are characterized by

$$I(t) = I_c \sin \varphi(t) \tag{2.19}$$

$$\frac{\partial \varphi}{\partial t} = \frac{2eV(t)}{\hbar} \tag{2.20}$$

where I_c is the critical current (the maximum current supported by the junction), φ is the phase across the junction, e is the electron charge, and $\hbar$ is the reduced Planck constant.

The critical current is given by

$$I_c = \frac{2e}{\hbar} E_J \tag{2.21}$$

where E_J is the Josephson coupling energy, which characterizes how easily Cooper pairs can tunnel through the junction [22].

Defining the magnetic flux quantum as

$$\Phi_0 = \frac{h}{2e} \tag{2.22}$$

and reduced magnetic flux quantum as

$$\phi_0 = \frac{\hbar}{2e}, \tag{2.23}$$

we can rewrite the critical current as

$$I_c = \frac{E_J}{\phi_0} = 2\pi \frac{E_J}{\Phi_0} \tag{2.24}$$

The reader may refer to the classic text [23] for a thorough discussion on superconductivity.

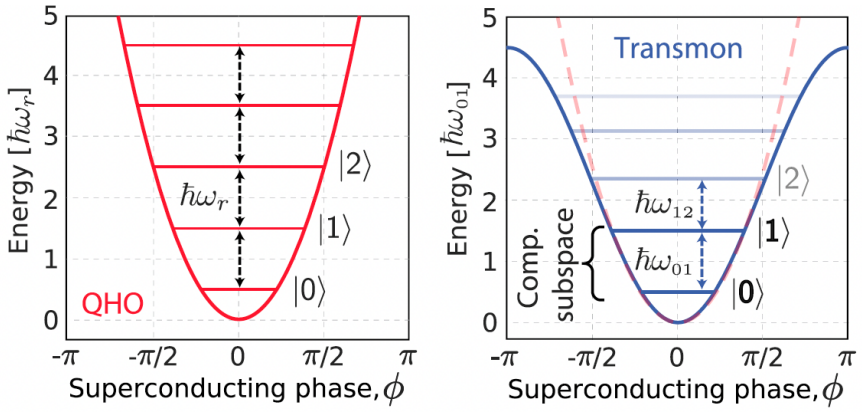

Figure 2-3: (left) Eigenenergies of an LC oscillator. (right) Eigenenergies of a transmon qubit. Figure from [24].

2.3 The Superconducting Qubit

The LC oscillator on its own cannot form a qubit, as all energy levels are equally spaced (see Fig. 2-3). Thus, we need to introduce nonlinearity via the Josephson junction.

Let us consider a Josephson junction with Josephson energy E_J shunted with a capacitance C. The capacitance sets the charging energy E_C, defined as

$$E_{\mathrm{C}} = \frac{e^2}{2C_\Sigma} \tag{2.25}$$

where $C_\Sigma = C + C_J$, and C_J is the junction capacitance.

Using (2.20), we can find that the phase angle across the junction φ is directly proportional to the flux variable ϕ used for the quantized LC oscillator (which we now refer to as Φ).

$$\varphi = \frac{2e}{\hbar}\Phi = 2\pi\frac{\Phi}{\Phi_0} \tag{2.26}$$

Much like the LC oscillator, we can define a Lagrangian and Hamiltonian [22]

$$\mathcal{L} = \frac{1}{2}C\dot{\Phi}^2 + E_{\mathrm{J}}\cos\left(2\pi\frac{\Phi}{\Phi_0}\right) \tag{2.27}$$

$$H = \frac{1}{2C}Q^2 - E_{\mathrm{J}}\cos\left(2\pi\frac{\Phi}{\Phi_0}\right) \tag{2.28}$$

Taking the cosine to lowest order (and ignoring the constant), we can approximate the Hamiltonian as

$$H \approx \frac{1}{2C}Q^2 + \frac{1}{2L_{\mathrm{J}}}\Phi^2 \tag{2.29}$$

where we approximate the small-signal effective inductance of the Josephson junction to be

$$L_{\mathrm{J}} = \left(\frac{\hbar}{2e}\right)^2 \frac{1}{E_{\mathrm{J}}} \tag{2.30}$$

In this small-signal limit, the Josephson plasma frequency, or resonant frequency, of this transmon is

$$\Omega_{\mathrm{J}} \equiv \frac{1}{\sqrt{L_{\mathrm{J}}C}} = \frac{1}{\hbar}\sqrt{8E_{\mathrm{J}}E_{\mathrm{C}}} \tag{2.31}$$

In the general case (no small-signal), the flux-dependent effective inductance is

$$L^{-1}(\Phi) \equiv \frac{d^2H}{d\Phi^2} = E_{\mathrm{J}}\left(\frac{2\pi}{\Phi_0}\right)^2 \cos\left(2\pi\frac{\Phi}{\Phi_0}\right) \tag{2.32}$$

In the limit where $E_J >> E_C$, we call the qubit a "transmon" [25]. In this limit, the transmon is very insensitive to charge fluctuations and can maintain longer coherence, but the anharmonicity is reduced. Nonetheless, the transmon limit has become the favored regime of operation since the charge dispersion decreases exponentially with E_J/E_C, whereas the anharmonicity decreases by a weak power law with E_J/E_C [25].

2.4 Black Box Quantization

Since the transmon is a weakly anharmonic oscillator, it lends itself to semiclassical forms of analysis that quantize linear circuits. A useful method for analyzing weakly anharmonic superconducting circuits is black box quantization [26, 27]. By replacing the Josephson junction with a linear inductor and computing the admittance $Y(\omega)$ seen looking into the terminals of the junction, the resonance frequencies, quality factors, self-Kerrs, and cross-Kerrs of the system can be calculated. We might model the impedance $Z(\omega)$ looking into the terminals of the junction as a combination of capacitors, inductors, and resistors.

$$Z(\omega) = \sum_{p=1}^{M} \left(j\omega C_p + \frac{1}{j\omega L_p} + \frac{1}{R_p} \right)^{-1} \tag{2.33}$$

The resonance frequencies are the real parts of the zeros of the admittance $Y(\omega) = Z(\omega)^{-1}$. If the circuit has weak dissipation (i.e, the resistances are much larger than the characteristic impedance, $R_p >> \sqrt{L_p/C_p}$), then the eigenmodes are given by

$$\omega_p = \frac{1}{\sqrt{L_p C_p}}. \tag{2.34}$$

The effective resistance is given by $R_p = 1/\mathrm{Re}Y(\omega_p)$ and effective capacitance by $C_p = \frac{1}{2}\mathrm{Im}Y'(\omega_p)$. Combining the two gives us the quality factor of each mode

$$Q_p = \frac{\omega_p}{2} \frac{\mathrm{Im}\, Y'(\omega_p)}{\mathrm{Re}\, Y(\omega_p)}. \tag{2.35}$$

Similarly, the self-Kerr, or anharmonicity, of each mode is given by

$$\chi_{pp} = -\frac{L_p}{L_J} \frac{C_J}{C_p} E_C \tag{2.36}$$

and the cross-Kerr between two modes by

$$\chi_{pp'} = -2\sqrt{\chi_{pp}\chi_{p'p'}}. \tag{2.37}$$

Note that this expression for cross-Kerr does not consider higher-order effects in anharmonicity, notably the straddling regime where $\chi_{pp'} > 0$ [25, 26].

2.5 Dispersive Readout

We finally arrive at circuit quantum electrodynamics (cQED) [10, 11, 28]. As is often convention, we will drop $\hbar$ in our discussion.

The Jaynes-Cummings Hamiltonian describes the interaction of an atom (qubit)

in a cavity (resonator).

$$H_{JC} = \frac{1}{2}\omega_{\mathrm{q}}\sigma_z + \omega_r\left(a^\dagger a + \frac{1}{2}\right) + g\left(\sigma_+ a + \sigma_- a^\dagger\right) \tag{2.38}$$

where ω_q is the bare resonant frequency of the qubit, ω_r is the bare resonant frequency of the resonator, σ_z is the Pauli-z operator, σ_+ is the raising operator, σ_- is the lowering operator, a and $a^\dagger$ are the annihilation and creation operators, and g is associated with the dipole matrix element connecting the ground and excited states of the atom.

The region of operation where the detuning Δ between the qubit and resonator is very large compared with coupling rate g and resonator linewidth κ ($\Delta >> g, \kappa$) is known as the "dispersive" limit. In this limit, the Jaynes-Cummings Hamiltonian reduces to

$$H_{\mathrm{disp}} = (\omega_r + \chi\sigma_z)\left(a^\dagger a + \frac{1}{2}\right) + \frac{\tilde{\omega}_{\mathrm{q}}}{2}\sigma_z \tag{2.39}$$

From this expression, we see that the resonator experiences a qubit-state-dependent frequency shift. We can thus infer the state of the qubit by probing at the resonator frequency and observing the qubit-state-dependent dispersive phase shift on the probing signal. While there have been proposals for longitudinal coupling [29, 30] and non-perturbative cross-Kerr [31], this dispersive readout has become the favored method of quantum nondemolition (QND) measurement.

By rewriting this expression, we can interpret the qubit-resonator interaction in another way [24]

$$H_{\mathrm{disp}} = \omega_r\left(a^\dagger a + \frac{1}{2}\right) + \frac{1}{2}(\omega_{\mathrm{q}} + \underbrace{\frac{g^2}{\Delta}}_{\text{Lamb shift}} + \underbrace{\frac{2g^2}{\Delta}a^\dagger a}_{\text{ac-Stark shift}})\sigma_z \tag{2.40}$$

The bare qubit frequency is first shifted by a fixed g^2/Δ, known as the "Lamb shift." However, it is also shifted by an amount proportional to the number of photons populating the resonator, known as the "ac-Stark shift."

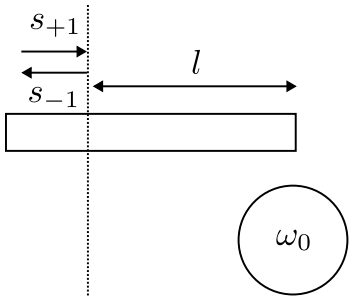

Figure 2-4: Single-mode standing wave resonator coupled to one-sided waveguide.

In the two-level approximation of the qubit, the dispersive shift χ is given by [10]

$$\chi \approx \frac{g^2}{\omega_q^b - \omega_r^b} \tag{2.41}$$

where the bare qubit and resonator frequencies are given by ω_q^b and ω_r^b.

For a transmon, the dispersive shift is instead given by [19]

$$\chi \approx -\frac{g^2 \delta_q}{\left(\omega_q^b - \omega_r^b\right)\left(\omega_q^b - \delta_q - \omega_r^b\right)} \tag{2.42}$$

where δ_q is the qubit anharmonicity ($\delta_q > 0$).

Typically, the resonator decay rate is matched to the cross-Kerr to provide maximum qubit measurement pointer separation [29].

$$\chi = \frac{\kappa}{2} \tag{2.43}$$

2.6 Forms of Readout

Quantum measurement chains typically use some form of either reflection or transmission readout. As will be explained in Sec. 3.1, transmission readout is likely more scalable in the long term. First, we will derive the response of both forms of readout using coupled mode theory [32].

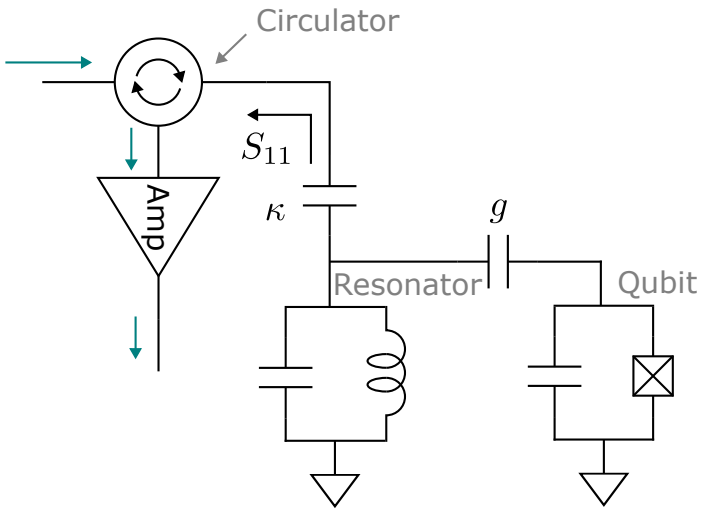

Figure 2-5: Reflection measurement. A circulator is needed to redirect the input signal to the traveling wave parametric amplifier (TWPA).

2.6.1 Reflection

A reflection measurement uses a one-sided cavity, or equivalently, a single-ended transmission line that is terminated by the resonator-qubit system (see Fig. 2-5).

We can determine the response of this system by coupled mode theory analysis [32], as a standing wave resonator supporting a mode with amplitude a coupled to a single-sided waveguide, as shown in Fig. 2-4. We can consider this mode to have resonant frequency ω_o, amplitude a, and energy $|a|^2$. If the resonator has a high quality factor, we can consider only the lowest order mode of the waveguide and ignore dispersion. Like in S-parameter analysis, we consider an incident (reflected) power wave with amplitude s_{+1} (s_{-1}). The power carried by the wave s_{+1} is $|s_{+1}|^2$. The evolution of the resonant mode in time is given by (2.44), where $1/\tau_o$ is the unloaded resonator decay, $1/\tau_e$ is the total external decay of the resonator into the waveguide, κ is the coupling coefficient between a and the forward propagating modes in the waveguide. The internal (or unloaded) quality factor of the resonator is given by $Q_i = \omega_o \tau_o/2$ and the external (or loaded) quality factor is given by $Q_e = \omega_o \tau_e/2$.

$$\frac{da}{dt} = j\omega_o a - \left(\frac{1}{\tau_o} + \frac{1}{\tau_e}\right)a + \kappa s_{+1} \tag{2.44}$$

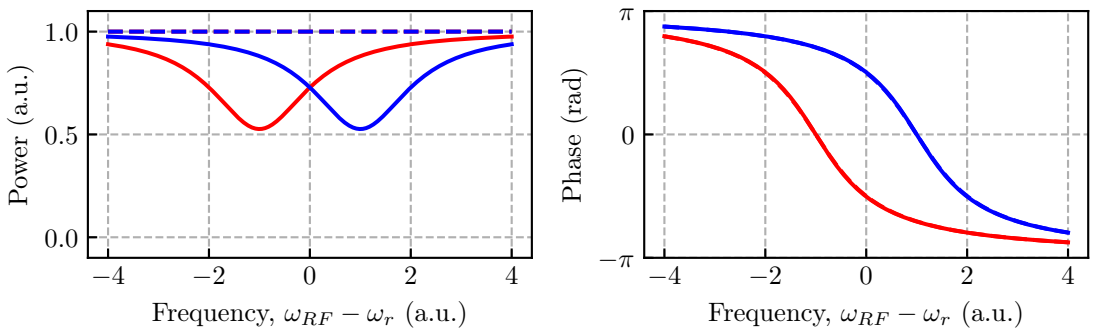

Figure 2-6: S_{11} of one-sided waveguide coupled to a lossless ($Q_i = \infty$, dotted lines) and lossy ($Q_i = 2000$, solid lines) readout resonator with qubit state-dependent response.

We can derive the time evolution of the mode as

$$a = \frac{\kappa s_{+1}}{j(\omega - \omega_o) + \frac{1}{\tau_o} + \frac{1}{\tau_e}}. \tag{2.45}$$

The reflection coefficient Γ, or equivalently S_{11}, can be found to be

$$S_{11} = \frac{s_{-1}}{s_{+1}} = \frac{1/\tau_e - 1/\tau_o - j(\omega - \omega_o)}{1/\tau_e + 1/\tau_o + j(\omega - \omega_o)}. \tag{2.46}$$

The qubit state-dependent reflected power and phase shift are shown in Fig. 2-6, where the dispersive shift of the qubit is set to half the decay rate of the resonator into the waveguide ($\chi = \kappa/2$) for maximum visibility.

2.6.2 Transmission

A transmission measurement uses a two-sided cavity, or a resonator coupled to a two-sided waveguide. In the following analysis, we will see that much of the signal is reflected. For this reason, qubit readout is often implemented with a weakly-coupled port (in the form of a small capacitance) such that the majority of the signal is transmitted [20], such as in Fig. 2-8.

Like with reflection measurement, we can analyze the response of this system with coupled mode theory, as a standing wave mode a coupled to a two-sided (or

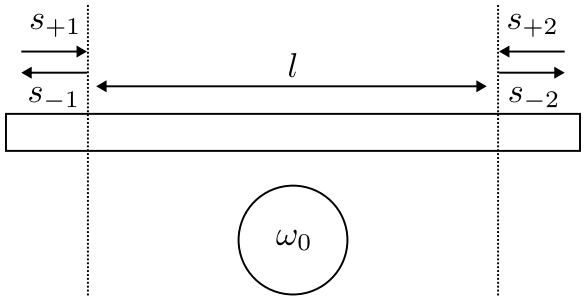

Figure 2-7: Single-mode standing wave resonator coupled to a two-sided waveguide.

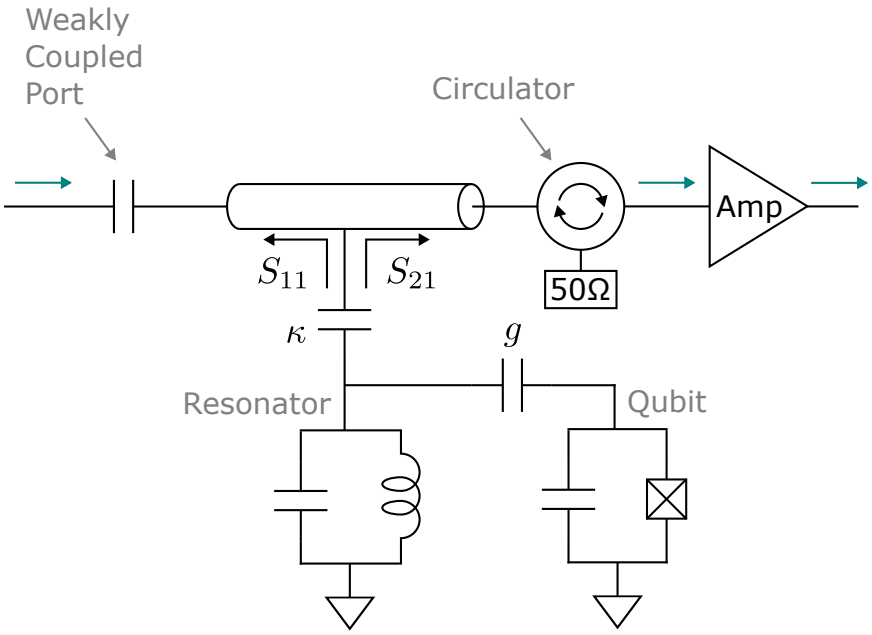

Figure 2-8: Transmission measurement with weakly-coupled port. Note, the need for a circulator for impedance matching to the amplifier.

open) waveguide, as shown in Fig. 2-7. Note, we will omit the weakly-coupled port in the analysis, and simply determine S_{21} and S_{11} as denoted in Fig. 2-8. We assume the resonator interacts with the forward and backward propagating modes of the waveguide. We now consider incident (reflected) power waves with amplitude s_{+1} (s_{-1}) and s_{+2} (s_{-2}), respectively. The evolution of the resonant mode in time is given by (2.47), with the same variable definitions as before with the addition that κ_1 is the coupling coefficient between a and forward propagating modes, and κ_2 is the coupling coefficient between a and backward propagating modes.

$$\frac{da}{dt} = j\omega_o a - \left(\frac{1}{\tau_o} + \frac{1}{\tau_e}\right)a + \kappa_1 s_{+1} + \kappa_2 s_{+2} \tag{2.47}$$

The total external decay satisfies the following relation, where $1/\tau_{e1}$ is the decay of the resonator in the forward direction and $1/\tau_{e2}$ is the decay in the backward direction.

$$\frac{2}{\tau_e} = \frac{1}{\tau_{e1}} + \frac{1}{\tau_{e2}} \tag{2.48}$$

We can find from time-reversal symmetry that the relation between the decay and the coupling coefficient is given by (2.49).

$$\kappa_i = \sqrt{\frac{1}{\tau_{e_i}}} e^{j\theta_i} \tag{2.49}$$

Power conservation dictates that the reflected waves are given by

$$s_{-1} = e^{-j\beta l}(s_{+2} - \kappa_2^* a) \tag{2.50}$$

$$s_{-2} = e^{-j\beta l}(s_{+1} - \kappa_1^* a) \tag{2.51}$$

Assuming that s_{+1} has a form $e^{j\omega t}$ and $s_{+2} = 0$, then the steady state of the mode evolution can be derived to be

$$a = \frac{\sqrt{\frac{1}{\tau_{e1}}} e^{j\theta_1} s_{+1}}{j(\omega - \omega_o) + \frac{1}{\tau_o} + \frac{1}{\tau_e}} \tag{2.52}$$

and (2.50) and (2.51) become

$$s_{-1} = -e^{-j\beta l} \sqrt{\frac{1}{\tau_{e2}}} e^{-j\theta_2} a \tag{2.53}$$

$$s_{-2} = e^{-j\beta l}\left(s_{+1} - \sqrt{\frac{1}{\tau_{e1}}} e^{-j\theta_1} a\right) \tag{2.54}$$

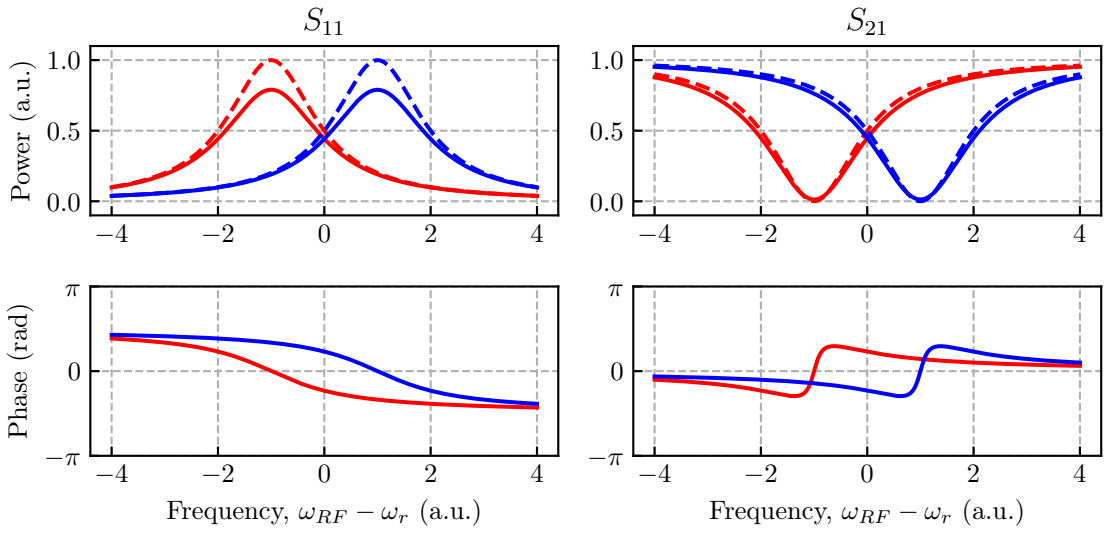

Figure 2-9: Scattering parameters of transmission measurement of open waveguide coupled to lossless ($Q_i = \infty$, dotted lines) and lossy ($Q_i = 2000$, solid lines) readout resonator with qubit state-dependent response. S_{11} and S_{21} refer to the notation used in Fig. 2-8, as though the weak coupling capacitor was absent.

Substituting (2.52) into (2.53)-(2.54), we get the following scattering parameters.

$$S_{11} = \frac{s_{-1}}{s_{+1}} = -e^{-j\beta l} \frac{\sqrt{\frac{1}{\tau_{e1}\tau_{e2}}} e^{j(\theta_1 - \theta_2)}}{j(\omega - \omega_o) + \frac{1}{\tau_o} + \frac{1}{\tau_e}} \tag{2.55}$$

$$S_{21} = \frac{s_{-2}}{s_{+1}} = e^{-j\beta l} \left(1 - \frac{\frac{1}{\tau_{e1}}}{j(\omega - \omega_o) + \frac{1}{\tau_o} + \frac{1}{\tau_e}} \right) \tag{2.56}$$

If we assume resonance $\omega = \omega_o$, neglect loss $1/\tau_o = 0$, and that the phase of coupling to the waveguide is equal for forward and backward propagating waves $\theta_1 = \theta_2$, we find from (2.48) and (2.55)-(2.56) that $S_{11} = -1$ and $S_{21} = 0$, as we would expect from a waveguide coupled to a resonator.

The qubit state-dependent scattering parameters are shown in Fig. 2-9, where the dispersive shift of the qubit is set to half the decay rate of the resonator into the waveguide ($\chi = \kappa/2$) for maximum visibility. Note that in this case, $|S_{11}|^2 = 0.5$ and $|S_{21}|^2 = 0.5$, if we probe at the resonator frequency $\omega_{RF} = \omega_r$.

2.7 Decoherence and Noise

The longitudinal relaxation rate is the rate of decay of the qubit from the excited to the ground state and is given by $1/T_1$, where T_1 is the longitudinal relaxation time. There are many decay channels, such as intrinsic material loss and Purcell decay, or decay of the qubit state into the waveguide.

The Purcell decay rate at which the qubit state decays into the waveguide is given by [10, 33]

$$\Gamma_p \approx \kappa \left(\frac{g}{\omega_q - \omega_r} \right)^2 \tag{2.57}$$

where κ is the resonator decay rate, or energy damping rate, that results predominantly from leakage into the transmission line. We'll refer to the Purcell-limited qubit lifetime as $T_{1,\text{Purcell}} = 1/\Gamma_p$.

The transverse relaxation time T_2 characterizes the dephasing rate of the qubit. It is often dominated by photon shot noise (from thermal or measurement photons).

The dephasing rate due to photon shot noise is given by [33, 34]

$$\Gamma_\varphi = \eta \frac{4\chi^2}{\kappa} \bar{n} \tag{2.58}$$

where

$$\eta = \frac{\kappa^2}{\kappa^2 + 4\chi^2} \tag{2.59}$$

If we operate at maximum visibility where $\chi = \kappa/2$, then the dephasing rate becomes directly proportional to the decay rate κ and photon number $\bar{n}$.

$$\Gamma_\varphi = \frac{1}{2} \kappa \bar{n} \tag{2.60}$$

2.8 Purcell Filters for Fast Readout

It is desirable to reduce gate time and measurement time, to maximize the number of operations that can be performed on a qubit during its coherence lifetime. To reduce measurement time, typically the resonator decay κ needs to be increased. However,

from (2.57), higher κ will also decrease the qubit lifetime and increase errors during qubit readout. At first, we may consider increasing the detuning between the qubit and resonator, but this would decrease χ, which from (2.43) needs to be on the order of κ for maximum visibility.

To overcome this trade-off, typical qubit readout designs include what is called a Purcell filter [18, 19], which aims to suppress Purcell decay. The design of this filter often aims to engineer the impedance environment from the perspective of the qubit and resonator.

We can restate this by viewing the resonator decay from two perspectives: (1) the perspective of the resonator κ and (2) the perspective of the qubit κ_q. To avoid confusion, κ_q is not the decay rate of the qubit Γ; it is the decay of the resonator as seen by the qubit. The Purcell suppression factor is given by κ/κ_q [19].

2.8.1 Bandpass Purcell Filter

A common implementation of a Purcell filter uses another lower-Q resonator at frequency ω_f to act as a bandpass filter [18, 19]. This filter resonator typically has a much lower quality factor Q_f (i.e, wider linewidth) and has very small detuning from the readout resonator ($\omega_f \approx \omega_r$). Due to the bandpass response where the peak is at ω_r, the coupling to the bus κ becomes frequency dependent, such that the κ_q is small and κ is large (see Fig. 2-10b).

Assuming $\omega_f \approx \omega_r$, the Purcell suppression factor of the bandpass filter is approximately given by [18]

$$\text{Purcell Suppression} \approx \left(\frac{2Q_f\Delta}{\omega_q}\right)^2 \tag{2.61}$$

where Δ is the detuning between qubit and resonator and Q_f is the external quality factor of the bandpass filter resonator. We see that the Purcell suppression is proportional to the square of the detuning and the quality factor of the filter resonator.

The bandpass Purcell filter could be implemented as an additional resonator interposed between the readout resonator and readout bus, as illustrated in Fig. 2-10a.

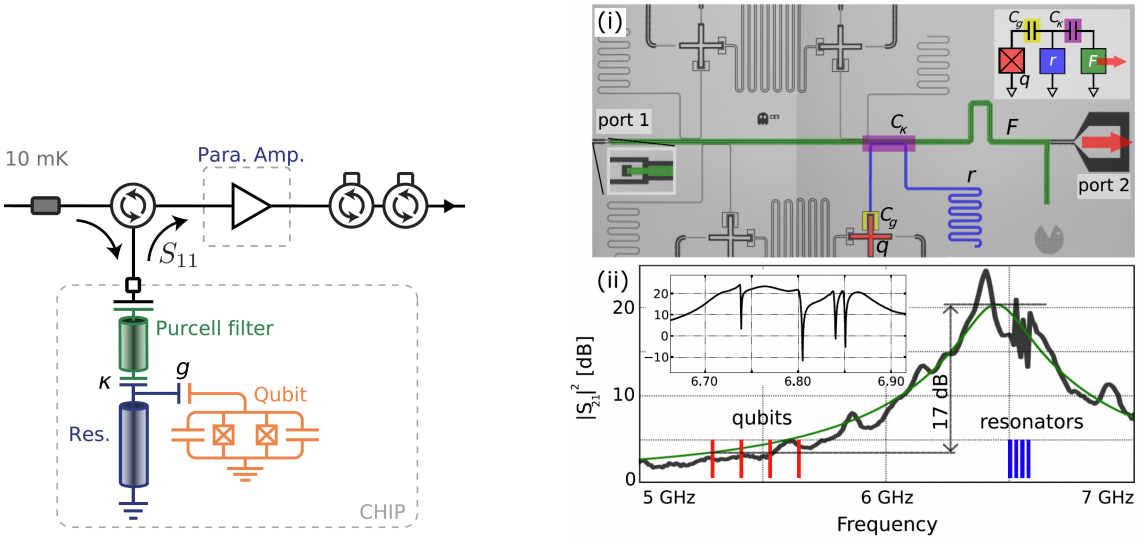

(a) (b)

Figure 2-10: (a) Example readout chain with bandpass Purcell filter as a resonator in series with the readout resonator. Figure adapted from [24]. (b) Physical layout of bandpass Purcell filter, showing micrograph of the device with lumped element model. Transmission spectrum of qubits and readout resonators are also depicted. Figure adapted from [18].

However, this approach is space-inefficient as a second transmission line resonator is needed for each qubit.

It is thus common to modify the bandpass Purcell filter to be shared by multiple readout resonators and serve the dual purpose of the readout bus [18]. This can be implemented by using a weakly-coupled port at one end of the readout line and a short stub termination at the other end such that the readout line is effectively a $\lambda/4$ resonator. See Fig. 2-10b for an example layout used in transmission readout. Note that this concept could be extended to reflection readout.

In the first demonstration of the bandpass Purcell filter [18], an expected Purcell suppression on the order of $\sim$100 is designed for[1], using $Q_f = 30$, $Q_r = 1561$, $g/2\pi = 86\,\text{MHz}$, $\kappa/2\pi = 4.3\,\text{MHz}$, and detuning of $1.2\,\text{GHz}$. This would correspond with an unfiltered qubit lifetime of $8\,\mu\text{s}$ and a filtered qubit lifetime of $1.2\,\text{ms}$. From Fig. 2-10b, we see that due to the bandpass design, this suppression exists over a very wide

[1]Since the goal is to make Purcell decay much smaller than other decay channels, experiments typically do not aim to observe the Purcell limit experimentally.

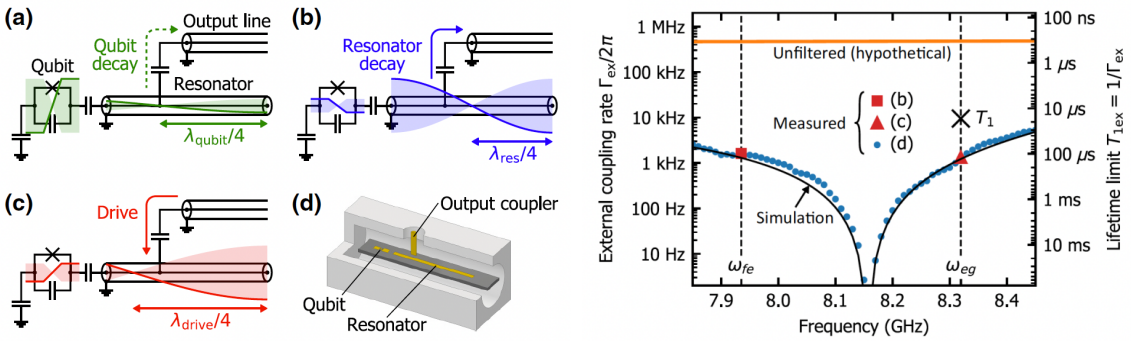

Figure 2-11: "Intrinsic" Purcell filter. Figures from [21]. (left) Distributed-element circuit models with voltage distributions for (a) dressed-qubit mode, (b) fundamental mode of the resonator, and (c) off-resonant drive. (d) Three-quarter section illustration of device. (right) The external qubit lifetime versus frequency.

bandwidth as long as the qubits are detuned by more than ∼1 GHz.

A further optimized design has targeted a Purcell suppression of ∼1340, using $Q_f = 74$, $Q_r = 126$, $g/2\pi = 208$ MHz, $\kappa/2\pi = 37.5$ MHz, and detuning of 1.6 GHz [35]. Note that if this was multiplexed readout, each readout resonator would need its own bandpass filter since Q_f and Q_r are much closer in magnitude, unlike in Ref. [18] where multiple resonators share one bandpass filter.

We will expand further on the limitations of the bandpass Purcell filter in the context of fast readout in Sec. 3.3.

2.8.2 "Intrinsic" Purcell Filter

Another approach has been proposed, called an "intrinsic" Purcell filter, in which the capacitive coupling of the output line to the readout resonator is positioned at the node of the dressed qubit voltage mode in the resonator, as in Fig. 2-11 [21]. The dressed qubit voltage mode is thus capacitively coupled to the point of minimum voltage, which will result in minimal decay.

In [21], for $g/2\pi = 224$ MHz, $\kappa/2\pi = 45.7$ MHz, and detuning of 2.2 GHz, a projected maximum Purcell suppression of more than 30,000 by aligning the qubit with the notch of the response (see Fig. 2-11). Due to the bandstop response, the "intrinsic" Purcell filter has a smaller bandwidth of suppression compared to the

bandpass filter. The bandwidth for which $T_{1,\text{Purcell}} > 1\,\text{ms}$ (corresponding to Purcell suppression of $\sim$3000) is more than 100 MHz.

Note, that although Fig. 2-11 depicts reflection-based measurement, this concept is more general and can be extended to transmission-based measurement as long as there is a weakly-coupled port that introduces standing-wave behavior which enables minimal coupling of the dressed qubit mode.

Chapter 3

Limitations of Typical Qubit Readout

In this section, we will discuss the limitations of current forms of readout and explain the need for a new form of Purcell suppression.

3.1 Scaling at the Fridge Level

As we saw in Sec. 2.6, conventional qubit readout architectures typically include some form of impedance mismatch, such as an "open" in the case of reflection measurement (Fig. 2-5) or a weakly-coupled port in transmission-based schemes (Fig. 2-8). The weakly-coupled port maximizes the directionality of qubit readout toward the output and minimizes loss to the input line [20]. Due to these impedance mismatches, a circulator is often needed[1] to impedance match the downstream amplifier. Impedance matching is often critical for traveling wave parametric amplifiers, which offer the large bandwidth necessary to perform multiplexed qubit readout [15, 16]. It is worth noting that the need for a circulator is a fundamental requirement of reflection readout since the output signal needs to be redirected from the input.[2]

Current superconducting qubit experiments use commercial bulky circulators with

[1] While the text refers to these non-reciprocal devices as circulators, note that in some cases such as transmission measurement, an isolator could also be used. Isolators can be replaced equivalently with a circulator with a matched termination at one port. Thus, for the sake of brevity, the text will refer to non-reciprocal elements generally as circulators, even though in some cases an isolator could also be used.

[2] For all forms of readout, an additional circulator is typically needed after the amplifier for noise protection, but that is not the focus of this discussion.

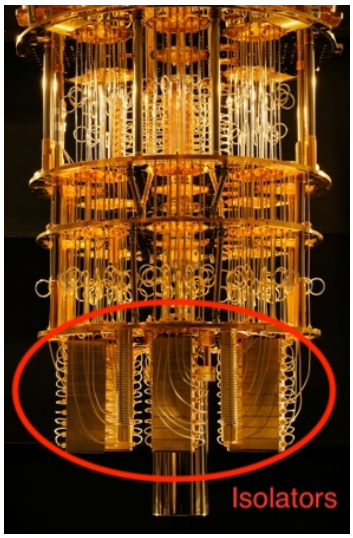

Figure 3-1: IBM's quantum computer. Figure from [36]. Note the amount of space occupied by isolators in the bottom stage.

permanent magnets to realize unidirectional signal flow. While prevalent and essential for current forms of qubit experiments, these non-reciprocal components are the largest, most massive, and highest magnetic-field components of a typical quantum measurement chain [24, 37]. Looking at the state-of-the-art quantum computers, high magnetic field components dominate the available space at the 10 mK plate (see an image of IBM's quantum computer in Fig. 3-1). There have been works investigating methods to integrate on-chip circulators using nonlinear parametric processes [38–40]. However, to date, no experimental realizations of a device with broad instantaneous bandwidth and sufficient isolation have been realized.

Estimates of the number of qubits needed for error correction are on the order of a million [41] and even the smallest commercial circulator has a volume on the order of tens of cubic centimeters. Assuming there is one non-reciprocal element for every ten qubits, the amount of space required for the circulators alone would still be on the order of several cubic meters! And this does not yet consider the cabling required to route each circulator to the qubits or the challenges associated with protecting the fragile qubits from such high magnetic field components. The motivation to reduce the number of circulators used is clear. Due to the fundamental need for a circulator in reflection measurement, the path forward likely lies with transmission readout if

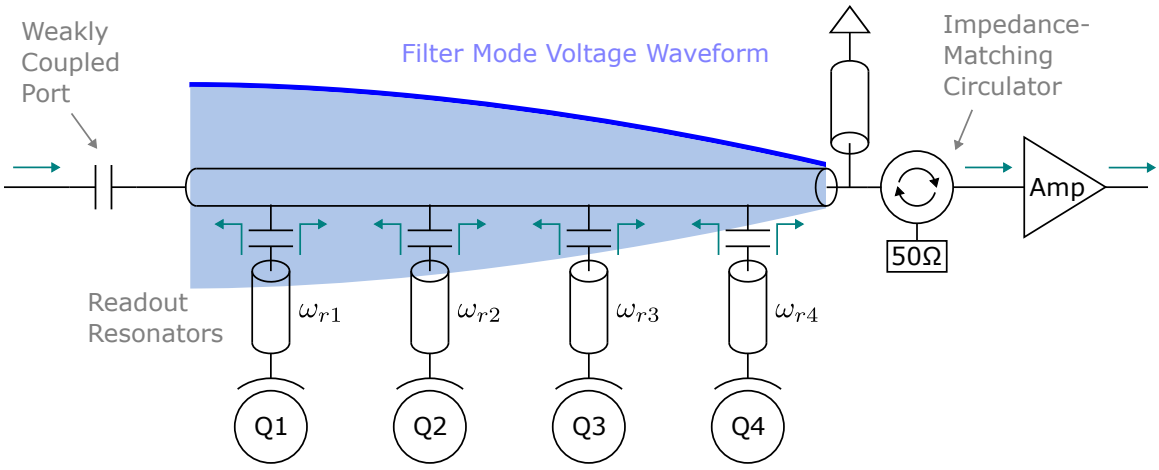

Figure 3-2: Typical multiplexed transmission readout setup, where the readout bus doubles as a $\lambda/4$ bandpass Purcell filter. Note that due to the filter mode's spatial dependence, each resonator decay must be designed according to the resonator's position along the readout bus. Also, note the need for an impedance-matching circulator due to the weakly-coupled port.

we are to minimize the number of circulators in the measurement chain.

3.2 Modularity at the Chip Level

In addition to requiring an impedance-matching circulator, "opens" and weakly-coupled ports also introduce challenges at the chip level; namely, they introduce standing-wave behavior. From our discussion in Sec. 2.8, these standing waves are at the heart of the success of the bandpass and "intrinsic" Purcell filters [18, 19, 21]. However, these standing waves also hinder design modularity, as they create a non-uniform impedance environment along the readout bus, as shown in Fig. 3-2. Since the dressed filter mode's voltage is different along the readout bus, each readout resonator that couples to this standing wave will have a different κ unless carefully designed for [18, 20, 35]. This spatial dependence and lack of modularity create headaches for chip designers as the design of each readout resonator-qubit system is also dependent on where it is positioned along the readout bus.

To correct this κ mismatch, the capacitive coupling of each resonator could be designed and tuned as part of the entire system, but this would require significantly

more time and computing resources for accurate modeling. An alternative approach spaces the readout resonators by $\lambda_r/2$ to couple each resonator to the antinode of the voltage waveform and uses a separate Purcell filter for each readout resonator [20]. However, this is less space-efficient since both extra $\lambda_r/2$ spacing and an additional filter resonator are needed for each qubit.

3.3 Faster Readout

The community is trending towards faster readout, especially for quantum error correction (QEC) [7–9]. Fault-tolerant protocols such as surface code have a cyclic nature where it is important to have a fast measurement time and rapid reset to minimize the collapse of the qubit state. To achieve faster measurement, the transient responses of readout resonators have continued to increase, enabling 99.2% fidelity in a readout time of 88 ns using a bandpass Purcell filter [35].

We now examine the limitations of the bandpass Purcell filter in the context of faster readout. We denote the linewidth of the readout resonator as κ_r given by

$$\kappa_r = \frac{\omega_r}{Q_r} \tag{3.1}$$

where Q_r is the external quality factor of the readout resonator. Note that the bandpass filter has a wider linewidth than the readout resonator, such that $Q_f < Q_r$. If multiple readout resonators share the same bandpass filter, then we must have $Q_f \ll Q_r$ so that multiple narrow-linewidth readout resonators can fit within the filter resonator's wide linewidth[18].

In the hybridized system of the Purcell filter and readout resonator, the transient response of the readout resonator that dictates the effective measurement rate is denoted by κ_{eff} and is given by [19]

$$\kappa_{\text{eff}} = \frac{4|\mathcal{G}|^2}{\kappa_{\text{f}}} \frac{1}{1 + (2\Delta_{\text{fd}}/\kappa_{\text{f}})^2} \tag{3.2}$$

where $\mathcal{G}$ is the coupling between the Purcell filter and resonator, Δ_{fd} is the detuning

between the filter frequency ω_f and the drive frequency ω_d, and $\kappa_f = \omega_f/Q_f$ is the Purcell filter linewidth. Note that κ_{eff} is dependent on the drive frequency. In this analysis, we will assume that we are driving at the resonator frequency, such that $\omega_d \approx \omega_f$ and thus $\kappa_{\text{eff}} \approx \kappa_r$ [19]. For this reason, κ_{eff} and κ_r can be used interchangeably in the rest of this section. We calculate the filtered Purcell decay by dividing the unfiltered Purcell decay in (2.57) by the Purcell suppression factor in (2.61).

$$\Gamma_p \approx \kappa_r \left(\frac{g}{\Delta}\right)^2 \left(\frac{\omega_q}{2Q_f\Delta}\right)^2 \tag{3.3}$$

where Δ is the detuning between the qubit and resonator. Observing that we must keep $Q_f < Q_r$ and substituting (3.1), we can arrive at the following inequality.

$$\Gamma_p > \kappa_r \left(\frac{g}{\Delta}\right)^2 \left(\frac{\omega_q}{2Q_r\Delta}\right)^2 = \kappa_r^3 \left(\frac{g}{\Delta}\right)^2 \left(\frac{\omega_q}{2\omega_r\Delta}\right)^2 \tag{3.4}$$

Keeping other factors constant[3], we see that $\Gamma_p > O(\kappa_r^3)$. This is because while the unfiltered Purcell decay formula (2.57) suggests that Γ_p should increase proportionally with κ_r, the bandpass Purcell filter introduces additional dependence since we are forced to keep Q_f less than $Q_r = \omega_r/\kappa_r$. Thus, for a bandpass Purcell filter, $T_{1,\text{Purcell}} < O(\kappa_r^{-3})$. Moreover, we note that the bandpass filter resonator has a practical limit of $Q_f \gtrsim 10$, since it will cease to demonstrate underdamped (i.e, resonant) behavior as Q_f approaches the critically damped value of $\frac{1}{2}$.

Instead of a bandpass filter, we can consider using a Purcell filter whose suppression is independent of κ. This κ-independent suppression is characteristic of the proposed "interference" Purcell filter, which will be discussed in Ch. 4. In this case, we are simply limited by (2.57), and thus $T_{1,\text{Purcell}} \sim O(\kappa_r^{-1})$. The caveat is that the suppression occurs over a more limited bandwidth, as we will show in the next chapter.

[3]Again, under the assumption of $\omega_d \approx \omega_r$ (so $\kappa_{\text{eff}} \approx \kappa_r$).

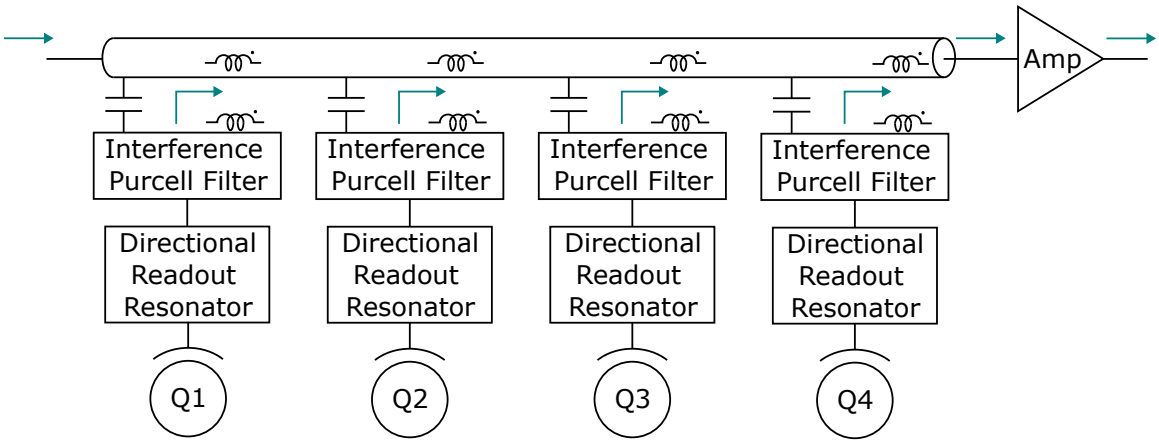

Figure 3-3: Vision of directional readout for improved modularity with no spatial dependence on the chip. Note, that no "open" or weakly-coupled port is used, so no impedance-matching circulator is needed.

3.4 A New Purcell Filter

To address the scaling and modularity challenges discussed in Sec. 3.1 and Sec. 3.2, we may consider a future quantum measurement chain with no "opens" or weakly-coupled ports (see Fig. 3-3). Such a design would avoid disturbing the impedance environment of the readout line, simultaneously precluding the need for an impedance-matching circulator and improving the modularity of many-qubit systems. To achieve the same directionality of transmission measurement as that with a weakly-coupled port, we envision a form of readout that uses "directional" resonators that demonstrate $|S_{21}|^2 = 1$ and $|S_{11}|^2 = 0$, without the reflection of a typical resonator coupled to a waveguide described in Sec. 2.6.2. A conceptual diagram of this readout is shown in Fig. 3-3.

From Fig. 3-3, implementing this directional readout would entail the development of several novel components. The remainder of this thesis will discuss the invention and design of one such component: a hardware-efficient Purcell filter that is compatible with this scalable and modular form of readout and that can be used for faster readout.

Chapter 4

Interference Purcell Filter

4.1 Operation

The proposed "interference" Purcell filter is depicted in Fig. 4-1. This filter is designed such that the qubit mode interferes destructively with itself in both the left and right directions along the readout transmission line.

The operation of this filter can be understood by following the waves at the qubit frequency from the qubit to each of the matched terminations. Across the mutual capacitance, the voltage experiences a $-90°$ phase delay while the current is in phase. Across the mutual inductance, the current experiences a $-90°$ phase delay while the voltage is in phase. The $\lambda_q/4$ waveguide introduces a $90°$ phase delay for both voltage and current. Thus, at the left matched termination, the voltage is out of phase and the current is in phase, so the power waves cancel. Likewise, at the right matched termination, the voltage appears in phase and the current out of phase, again resulting in power wave cancellation.

4.1.1 Generality

The use of interference to suppress Purcell decay is quite general and can be extended to other lengths of transmission line resonators and for other couplings. For example, the same effect can be generated by coupling a $\lambda_r/2$ resonator capacitively to

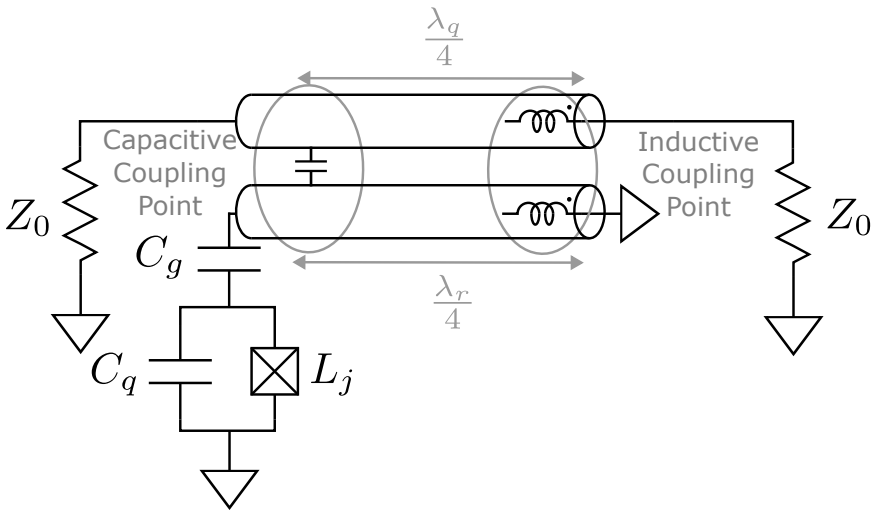

Figure 4-1: Proposed interference Purcell filter.

the waveguide at a separation of $\lambda_q/2$. Or, instead of capacitive coupling, in-phase inductive coupling could be used. However, either of these would effectively double the footprint of the design, so in this thesis, the smaller footprint design of Fig. 4-1 is investigated.

4.2 Modeling with SPICE

In this section, the simplified circuit model used for Simulated Program with Integrated Circuit Emphasis (SPICE) simulation is discussed.

Like other Purcell filters, the key is to engineer a different impedance environment from the perspective of the qubit compared to that of the readout resonator [18, 19]. The interference Purcell filter can be interpreted in much the same way. Since the qubit and resonator are at different frequencies, the interference is engineered to occur at the qubit frequency and has little practical effect at the resonator frequency.

The circuit model used for SPICE simulation is shown in Fig. 4-2. The impedance environment as seen by the qubit can be evaluated by looking at the scattering parameters, treating port 1 as the qubit and ports 2 and 3 as the left and right waveguide terminations. The circuit is modeled with a lumped LC resonator coupled to a waveguide with lumped mutual capacitance C_m and lumped mutual inductance L_m. The

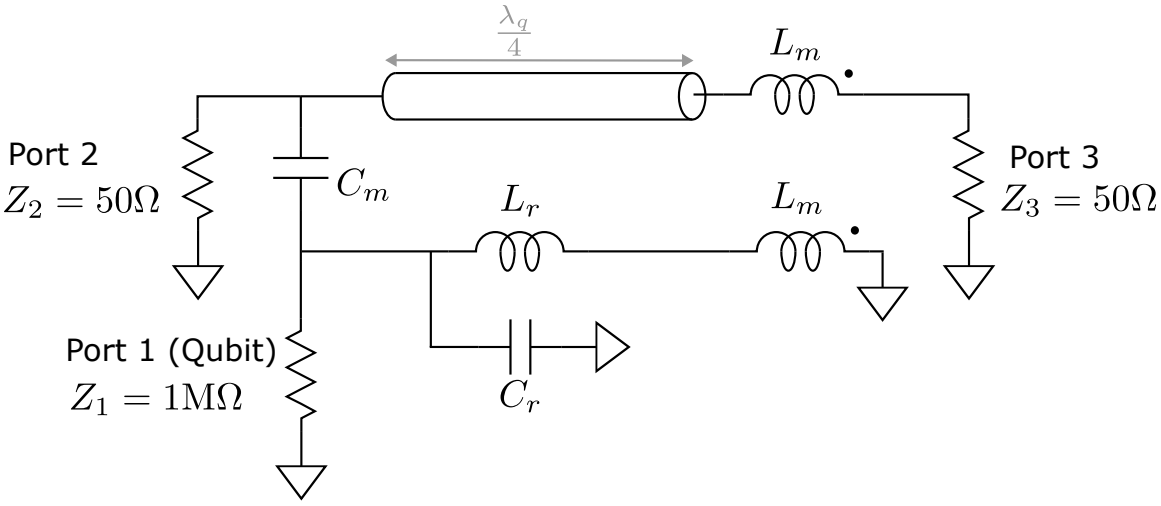

Figure 4-2: Circuit model of interference Purcell filter used for SPICE simulation with lumped couplings.

coupling coefficient for mutual inductance is assumed to be $k = 1$.

To keep the dressed resonator frequency the same for different C_m and L_m, the transmission line resonator is approximated as a bare lumped LC resonator with $L_{r,b}$ and $C_{r,b}$ given by

$$L_{r,b} = \frac{Z_r}{\omega_r} \tag{4.1}$$

$$C_{r,b} = \frac{1}{\omega_r Z_r} \tag{4.2}$$

where for a $\lambda/4$ resonator the impedance is given by

$$Z_r = \frac{4}{\pi} Z_0 \tag{4.3}$$

Since the design targets very fast measurement, the coupling magnitudes may be quite high. The lumped values are adjusted to account for the couplings C_m and L_m.

$$L_r = \frac{Z_r}{\omega_r} - L_m \tag{4.4}$$

$$C_r = \frac{1}{\omega_r Z_r} - C_m \tag{4.5}$$

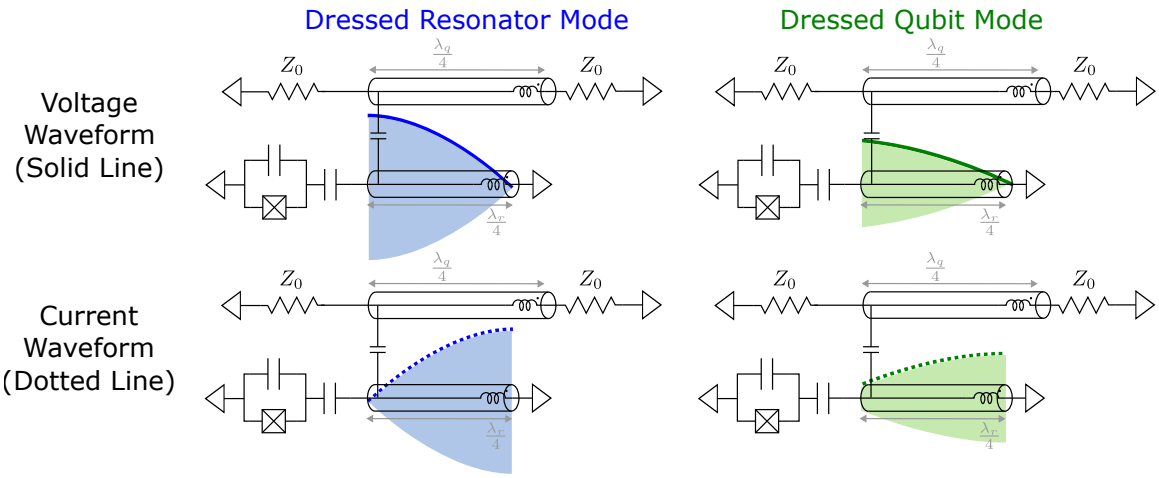

Figure 4-3: Dressed qubit and resonator modes with qubit positioned at resonator open. Voltage (solid lines) and current (dotted lines) waveforms are illustrated. Note that at the capacitive coupling point, the dressed qubit voltage waveform does not meet its maximum point, unlike the current waveform at the inductive coupling point.

4.2.1 Determining Optimal Parameters

To achieve the desired interference effect, the coupling magnitude at the qubit frequency needs to be matched at the two coupling points to maximize the destructive interference.

As a first pass, normalized capacitive and inductive couplings may be matched as

$$\frac{C_m}{C_o} = \frac{L_m}{L_o} \tag{4.6}$$

where L_m and C_m are the mutual inductance and capacitance and L_o and C_o are the distributed inductance and capacitance per unit length when the transmission lines are isolated from one another [42]. We will define the ratio of capacitive to inductive coupling to be $r_m = L_m/C_m$.

Note that this expression assumes that the voltage at the capacitive coupling point (V_{Cm}) and current at the inductive coupling point (I_{Lm}) satisfy

$$\frac{V_{Cm}}{I_{Lm}} = Z_0 \tag{4.7}$$

since the distributed inductance and capacitance can be found from the characteristic

impedance Z_0 of the two lines.

$$Z_0 = \sqrt{\frac{L_o}{C_o}} \tag{4.8}$$

If it is assumed that the qubit is located at the open of the $\lambda_r/4$ resonator[1], then (4.7) would only be satisfied if $\lambda_r = \lambda_q$, since V_{Cm} and I_{Lm} would be maximal at their respective points. Clearly, (4.7) is not a valid assumption for dispersive readout, since $|\lambda_r - \lambda_q| >> g, \kappa$ for the dispersive approximation to be valid. Nonetheless, we can use (4.6) to get an order of magnitude estimate.

Assuming $Z_0 = 50\,\Omega$, the distributed inductance to capacitance ratio would satisfy $L_o/C_o = 2.5\,\text{pH/fF}$. From (4.6), we expect the optimal ratio $r_{m,opt}$ to be on the same order of magnitude.

Eq. (4.7) can be better understood by visualizing the dressed qubit and resonator modes. If we assume $f_q < f_r$, then the dressed qubit and resonator modes would be of the shape shown in Fig. 4-3. Note that while the dressed resonator mode reaches its maximum $I_{Lm,r}$ and $V_{Cm,r}$, the dressed qubit mode only reaches a maximum $I_{Lm,q}$ but not $V_{Cm,q}$. To compensate for the smaller voltage at the capacitive coupling point, we would expect the necessary capacitance C_m to be larger than expected, and thus the optimal ratio $r_{m,opt}$ would be smaller than that as calculated from (4.6). As shown later in Fig. 4-4, we find this is indeed the case as $r_{m,opt} \approx 2.27\,\text{pH/fF} < 2.5\,\text{pH/fF}$.

4.2.2 Calculating Purcell Suppression from Transmission

In this section, the circuits will be modeled using $Z_0 = 50\,\Omega$ for the transmission lines and terminations and assuming $f_q = 5\,\text{GHz}$ and $f_r = 7\,\text{GHz}$. A port with a large impedance of $1\,\text{M}\Omega$ is used in place of the qubit to not disturb the modes of the resonator, while still simulating the transmission spectrum.

The Purcell suppression from our filter is estimated classically as

$$\text{Purcell Suppression} = \frac{|S_{21,\text{without filter}}|^2}{|S_{21,\text{with filter}}|^2} \tag{4.9}$$

[1]This initial assumption is made knowing that a transmon will be capacitively coupled to the resonator. It thus would not make sense to couple the qubit to the inductively coupled point since the voltage would be at a minimum there.

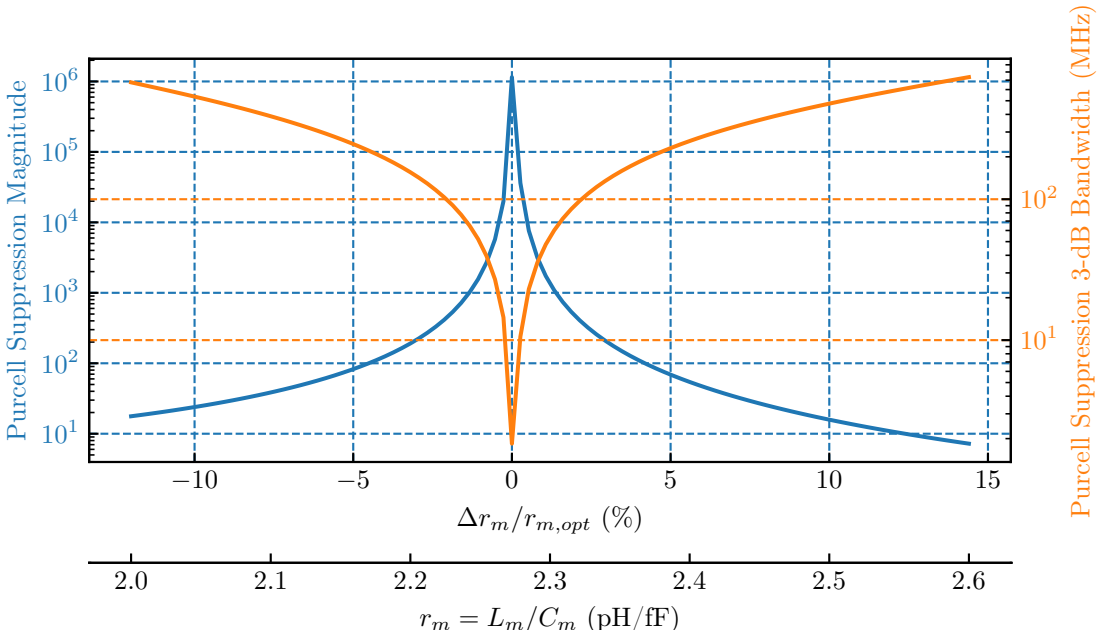

Figure 4-4: Purcell suppression magnitude and 3-dB bandwidth versus r_m.

where S_{21} is as indicated in Fig. 4-2. An equivalent analysis could be carried out with S_{31}, since $|S_{31}| = |S_{21}|$. The design without the interference Purcell filter is designed to match κ and uses purely capacitive coupling.

The Purcell suppression magnitude and full width at half maximum (FWHM) bandwidth were found for different ratios of r_m (see Fig. 4-4). The maximal Purcell suppression occurs at 2.27 pH/fF, matching our expectation that it would be lower than the initial estimate of 2.5 pH/fF. Fig. 4-4 is the same regardless of the choice of κ, demonstrating that this is a general result. This is because the Purcell suppression is dictated only by the interference effect, which is independent of κ. We will later again demonstrate this holds using circuit quantization (Sec. 4.3).

The spectrum of S_{21} is shown in Fig. 4-5, both with and without the interference filter. The transmission at the notch (the qubit frequency) is suppressed by more than 6 orders of magnitude. We can confirm the transmission near the resonator frequency is the same, validating that κ is the same.

To understand how sensitive the design is, the Purcell suppression is simulated for the optimal and non-optimal choice of r_m in Fig. 4-6. Reduction of the optimal

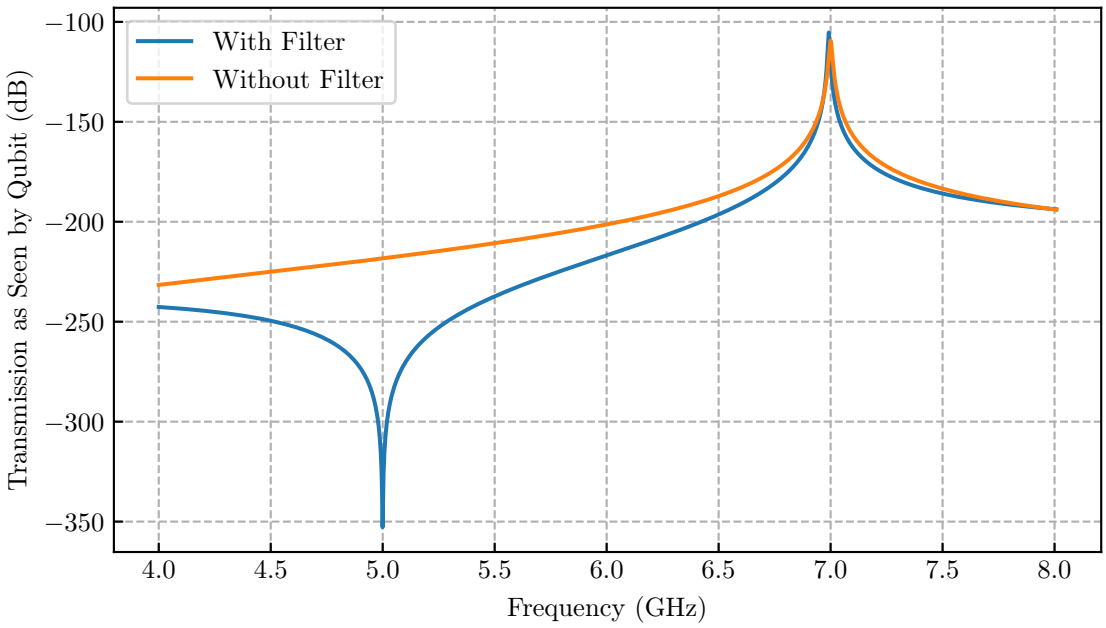

Figure 4-5: Transmission spectrum from the perspective of the qubit, where $r_m = r_{m,opt}$ and $\kappa/2\pi = 12.4\,\text{MHz}$.

ratio by 5% reduces the Purcell suppression to about 2.5 orders of magnitude.

4.3 Modeling with Circuit Quantization

The Quantum Circuit Analyzer Tool (QuCAT) [43] is used to model this circuit semi-classically with black box quantization.

Since at the time of writing, QuCAT can only take resistors, capacitances, and inductances, some approximations need to be made to our circuit model in Fig. 4-2. First, an equivalent circuit model is used for the mutual inductance. This is a valid model since, after swapping the position of the right-hand side series inductor and resistive termination, our circuit satisfies the port condition [44].

An appropriate T-network approximation can be used for the waveguide separation $\lambda_q/4$, valid at and around a certain frequency, which we take to be the qubit frequency at which the destructive interference occurs. The ABCD parameters are

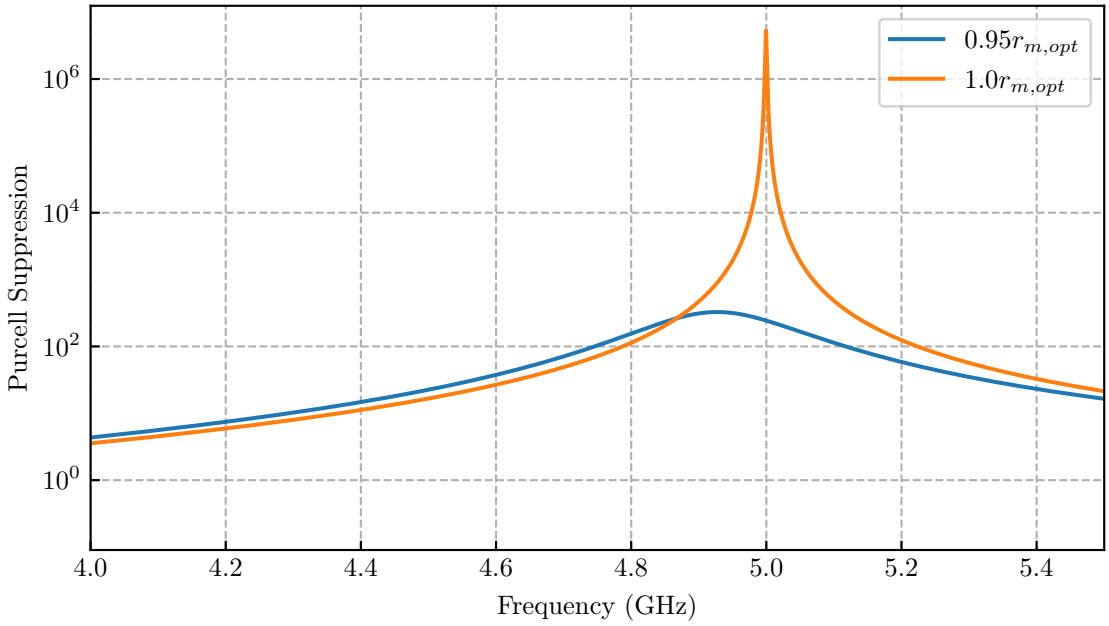

Figure 4-6: Purcell suppression spectrum from the perspective of the qubit, where $\kappa/2\pi = 12.4\,\text{MHz}$.

given by [44]

$$\begin{bmatrix} V_1 \\ I_1 \end{bmatrix} = \begin{bmatrix} A & B \\ C & D \end{bmatrix} \begin{bmatrix} V_2 \\ I_2 \end{bmatrix} \tag{4.10}$$

A T-network (shown in Fig. 4-7a) has the following ABCD parameters [44].

$$\begin{aligned} A &= 1 + \tfrac{Z_1}{Z_3} & B &= Z_1 + Z_2 + \tfrac{Z_1 Z_2}{Z_3} \\ C &= \tfrac{1}{Z_3} & D &= 1 + \tfrac{Z_2}{Z_3} \end{aligned} \tag{4.11}$$

Since a transmission line has the following ABCD parameters [44],

$$\begin{aligned} A &= \cos\beta\ell & B &= jZ_0 \sin\beta\ell \\ C &= jY_0 \sin\beta\ell & D &= \cos\beta\ell \end{aligned} \tag{4.12}$$

we can match the elements to (4.11) and derive an appropriate model for a length of $\lambda/4$.

The T-network is derived to represent a transmission line of length $\lambda/4$ at frequency ω using two series inductors L_{tml} and a shunt capacitor C_{tml} (see Fig. 4-7b).

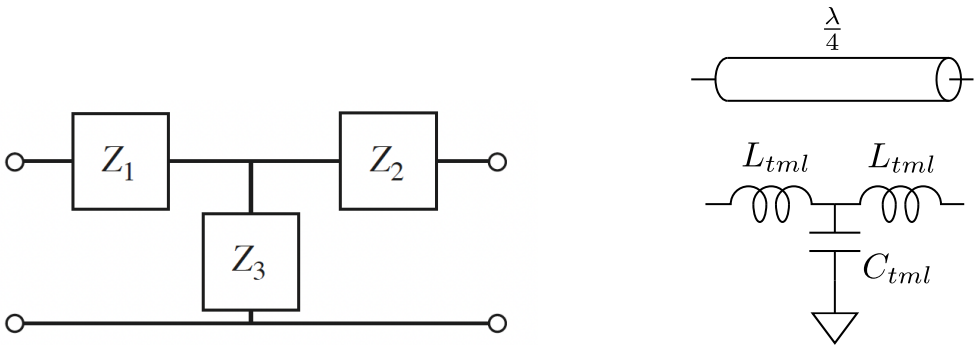

(a) (b)

Figure 4-7: (a) Two port network with 3 components in a T (or Y) configuration. (b) Approximation of $\lambda/4$ transmission line.

At the qubit frequency, the inductance and capacitance are given by

$$L_{tml,q} = \frac{Z_0}{\omega_q} \tag{4.13}$$

$$C_{tml,q} = \frac{1}{\omega_q Z_0} \tag{4.14}$$

The final model used in QuCAT is shown in Fig. 4-8, where the resonator decay is dictated by the couplings C_m and L_m, and the cross-Kerr, or dispersive shift, is largely determined by C_g, the coupling of the qubit to the resonator. This dependence on C_m, L_m, and C_g is plotted in Fig. 4-9.

4.3.1 Eigenmodes, Measurement Rate, and Dispersive Shift

Performance parameters are simulated with and without the interference Purcell filter. To provide a fair comparison, resonator and qubit eigenmodes ω_r, ω_q, resonator decay κ, and dispersive shift χ are matched between designs with and without the Purcell filter (see Fig. 4-9). The design without a Purcell filter is implemented such that the resonator is capacitively coupled to the waveguide.

Using the lumped circuit model in Fig. 4-8, the eigenmodes of the system can be found. Thus, black box quantization can be used to find the Purcell decay of the qubit and decay rates of the resonator. This also allows us to evaluate the approximations made in the previous section and to ensure that the system is behaving as expected.

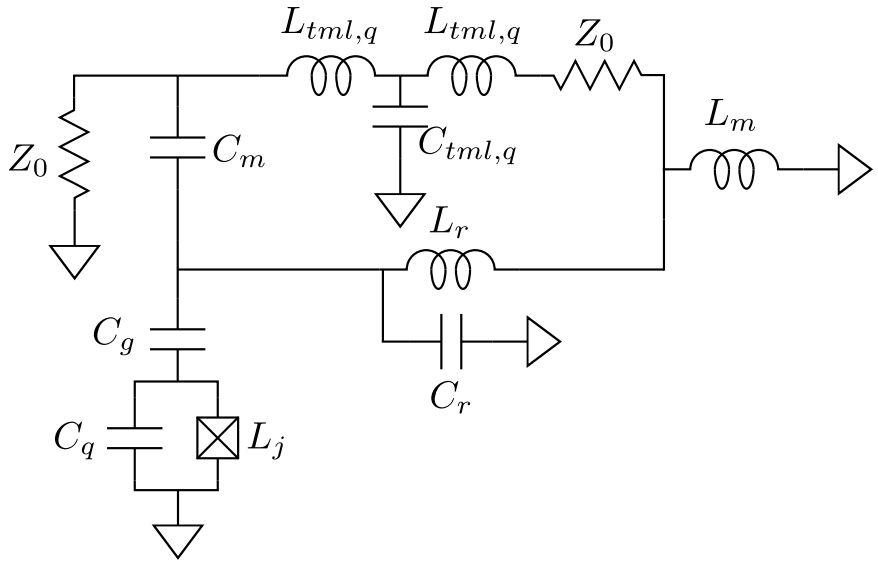

Figure 4-8: Interference Purcell filter with lumped couplings, transmission line approximation from ABCD parameters, transmission line resonator approximation, and equivalent model for mutual inductance.

4.3.2 Qubit Lifetime

Qubit lifetime is calculated from the Purcell decay Γ_p.

$$T_{1,\text{Purcell}} = \frac{1}{\Gamma_p} \tag{4.15}$$

The qubit lifetimes as a function of the qubit frequency are shown in Fig. 4-10. Note that the maximum increase in qubit lifetime is almost 6 orders of magnitude, similar to that predicted previously in Fig. 4-6.

The qubit lifetime is compared for different values of κ, where $\chi \approx \kappa/2$, ranging from 5 MHz to 15 MHz. For comparison, designs with r_m ratios at the optimal (dotted lines) and 5% from optimal (solid lines) were simulated (Fig. 4-11). From the figure, we see that the qubit lifetime decreases as κ is increased, as expected. Purcell suppression is calculated in a similar manner as before, now semiclassically, as

$$\text{Purcell Suppression} = \frac{T_{1,\text{Purcell, with filter}}}{T_{1,\text{Purcell, without filter}}}. \tag{4.16}$$

The Purcell suppression for different κ is plotted in Fig. 4-12. Note, that this plot

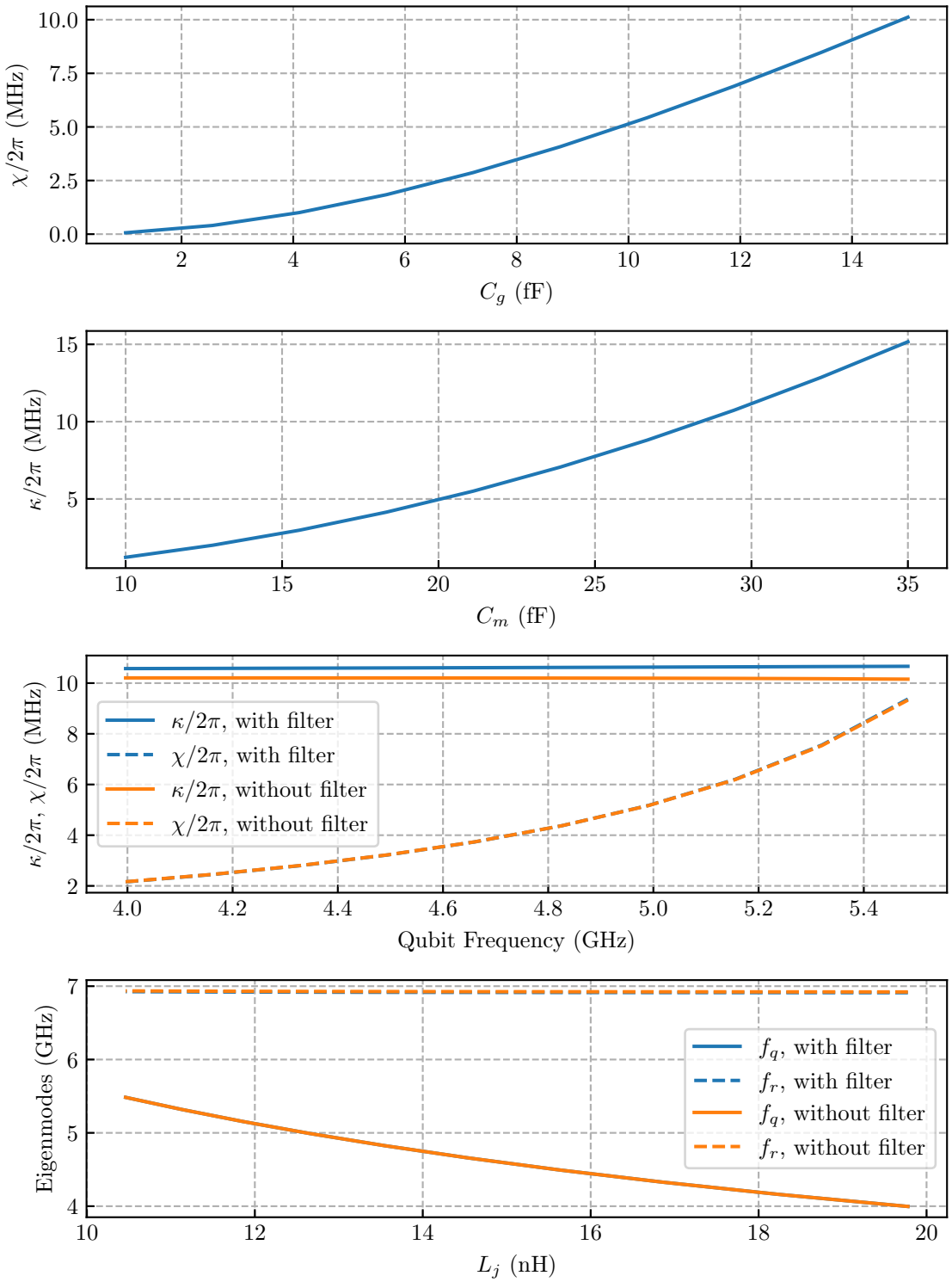

Figure 4-9: (a) Simulated cross-Kerr $\chi/2\pi$ versus C_g. (b) Simulated resonator decay $\kappa/2\pi$ for different C_m and L_m, scaled proportionally by ratio $r_{m,opt}$. (c) Simulated resonator decay $\kappa/2\pi$ and cross-Kerr $\chi/2\pi$ versus qubit frequency. (d) Simulated qubit and resonator eigenmodes versus L_j.

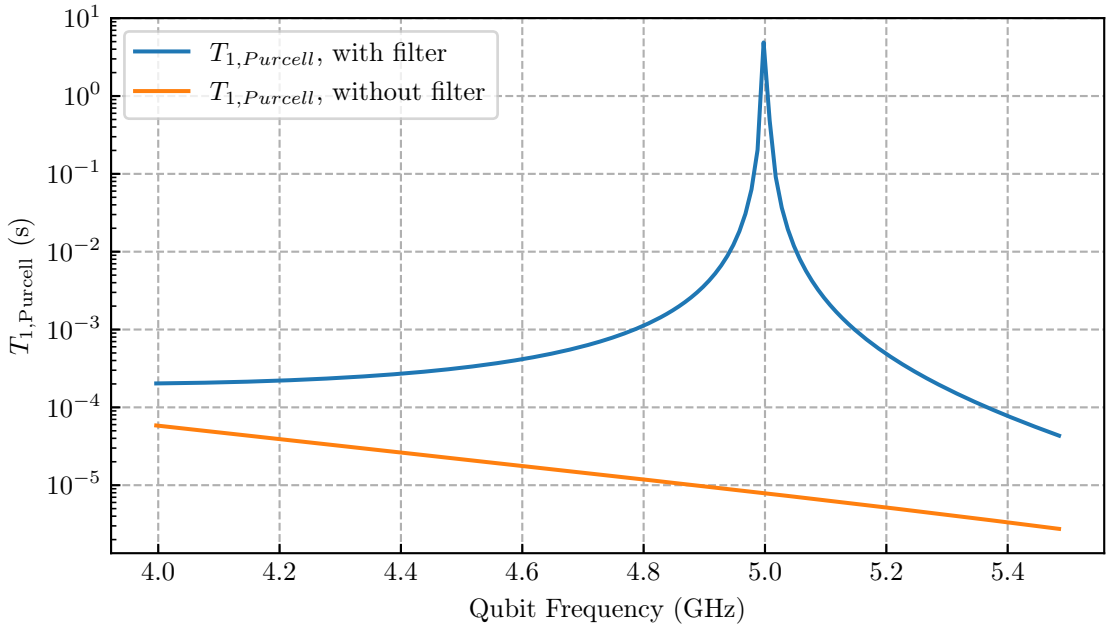

Figure 4-10: Comparison of unfiltered and filtered $T_{1,\mathrm{Purcell}}$.

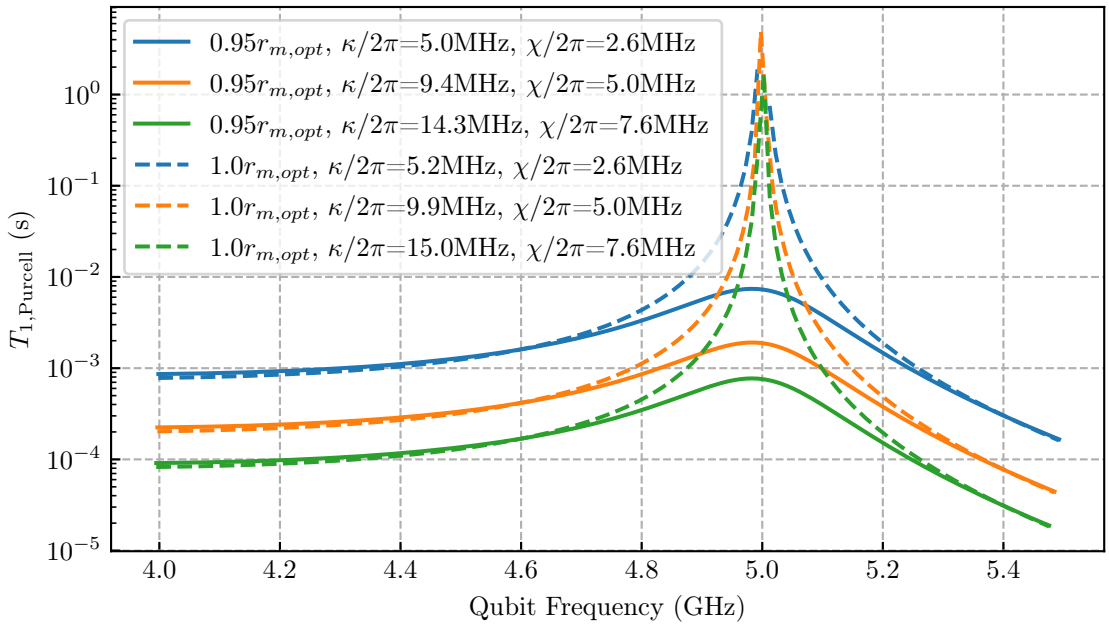

Figure 4-11: $T_{1,\mathrm{Purcell}}$ as a function of qubit frequency for a different κ (where $\chi \approx \kappa/2$), comparing the optimal ratio $r_{m,opt}$ and non-optimal ratio $r_m = 0.95r_{m,opt}$.

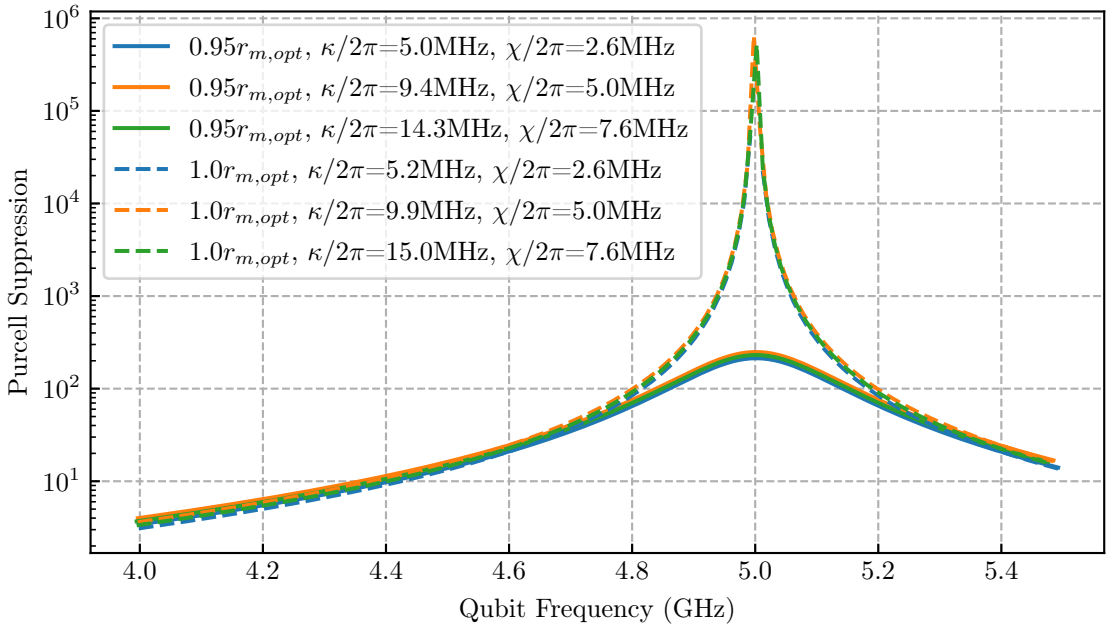

Figure 4-12: Purcell suppression as a function of qubit frequency for a different κ (where $\chi \approx \kappa/2$) comparing the optimal ratio $r_{m,opt}$ and non-optimal ratio of $0.95r_{m,opt}$. Note that the Purcell suppression is independent of the choice of κ. Note also that this result closely matches the result found from SPICE simulation that did not include the qubit in Fig. 4-6.

closely matches the Purcell suppression found from classical SPICE simulation in Fig. 4-6. Also, note again that the Purcell suppression is independent of the choice of κ.

Finally, the bandwidth above 1 ms is found as a function of κ and for optimal and non-optimal ratios of r_m (Fig. 4-13). If the optimal ratio is used, a bandwidth of more than 100 MHz can be maintained even for very large $\kappa/2\pi > 10$ MHz.

4.4 Electromagnetic Simulation

In this section, the physical layout of the interference Purcell filter is presented. Simulations are performed using Ansys High Frequency Simulation Software (HFSS).

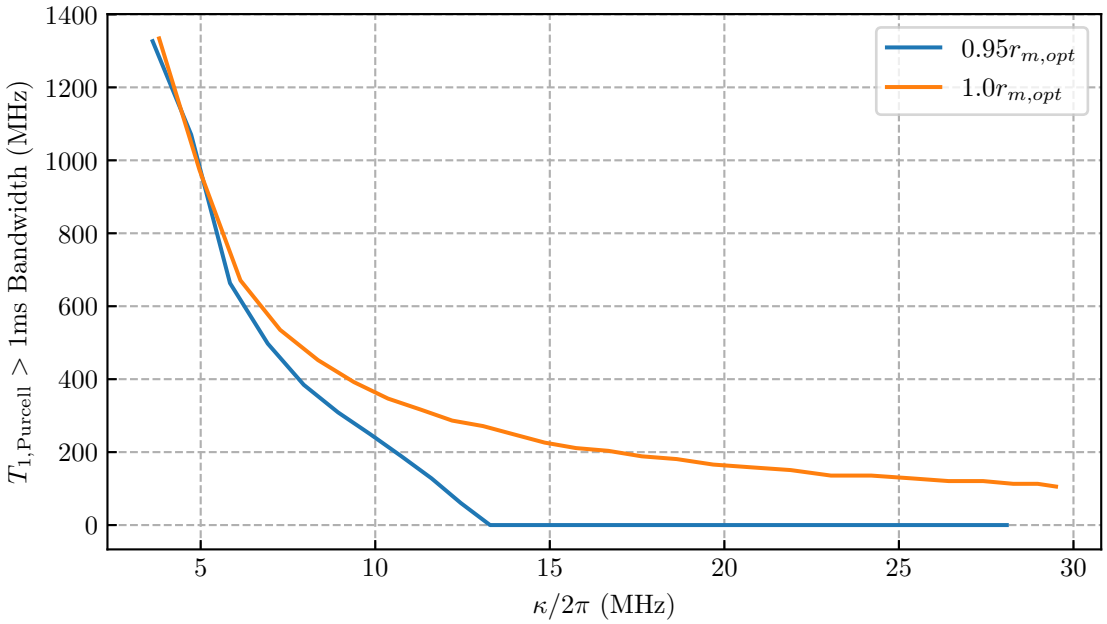

Figure 4-13: The qubit frequency bandwidth over which $T_{1,\text{Purcell}} > 1\,\text{ms}$ for different values of κ and ratio $r_m = L_m/C_m$.

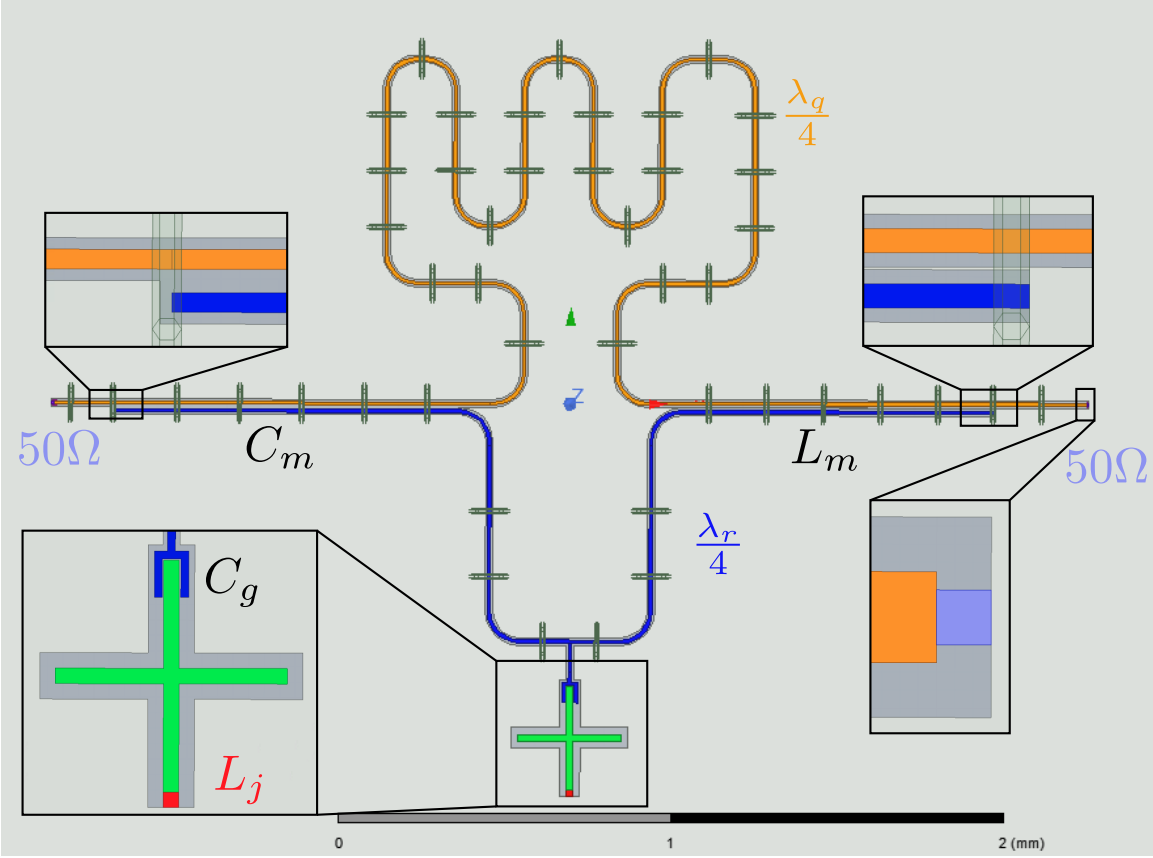

Figure 4-14: Physical layout of interference Purcell Filter.

4.4.1 Design

The layout is shown in Fig. 4-14. From a practical standpoint, it is beneficial to couple the qubit to the resonator in a manner that can keep it physically further from the readout bus, to mitigate parasitics that might exacerbate decay. The layout positions the qubit at the midpoint of the resonator and bends the resonator in a U-shape away from the bus.

The capacitive and inductive coupling are both implemented by coplanar waveguides (CPW), with a width of 10 µm and a gap of 6 µm. Capacitive coupling is implemented with a 1.09 mm coupling length and no ground spacing. Inductive coupling is implemented with a 1 mm coupling length and ground spacing of 1 µm.

The length ℓ of a $\lambda/4$ resonator (in blue) can be approximated by [45]

$$\ell \approx \frac{\lambda}{4} = \frac{\pi v}{2\omega} = \frac{\pi c}{2\omega\sqrt{\epsilon_{\text{eff}}}} \tag{4.17}$$

where c is the speed of light in vacuum and ϵ_{eff} is the effective relative dielectric constant of the CPW. Since the CPW dimensions are much smaller than the substrate thickness (350 µm), we can make the approximation

$$\epsilon_{\text{eff}} \approx \frac{1+\epsilon_s}{2}. \tag{4.18}$$

Using $\epsilon_s = 11.45$ for cryogenic silicon, $c = 3 \times 10^8$ m/s, and $\omega_r/2\pi = 7.6$ GHz, we expect a resonator length around 3.9 mm.

The Purcell decay into the readout bus (in orange) is modeled as a waveguide terminated in 50 Ω resistors (in purple). The $\lambda_q/4$ separation between the coupling points that is necessary for the destructive interference effect is meandered to keep the overall size small. Targeting a qubit frequency of $\omega_q/2\pi = 5.6$ GHz, from (4.17), the waveguide separation (not including the coupling interaction lengths) would be about 5.4 mm long.

A strong coupling $g/2\pi = 208$ MHz is achieved with a claw-like structure coupled to a transmon qubit (in green). The avoided crossing is depicted in Fig. 4-15. The

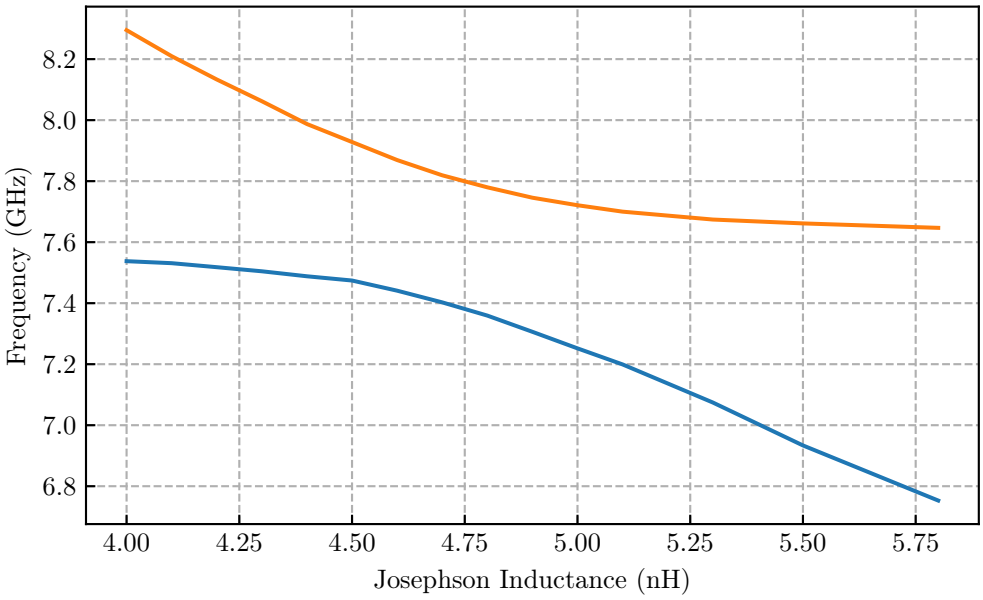

Figure 4-15: Avoided crossing of resonator and qubit modes, yielding a $g/2\pi = 208\,\text{MHz}$.

energy-participation ratio (EPR) [46] is used to find χ, yielding a value of $\chi/2\pi = -3.38\,\text{MHz}$.

4.4.2 Performance

Eigenmode simulation is performed, where the frequency ω and loaded quality factor Q are given for each eigenmode. The Josephson inductance is swept, just as the qubit frequency would be tuned in an experiment. The qubit and resonator eigenmodes are given in Fig. 4-15.

The resonator decay κ is simply given by

$$\kappa = \frac{\omega_r}{Q_r} \tag{4.19}$$

where Q_r is the loaded quality factor of the resonator mode. The design has a κ of about 15 MHz.

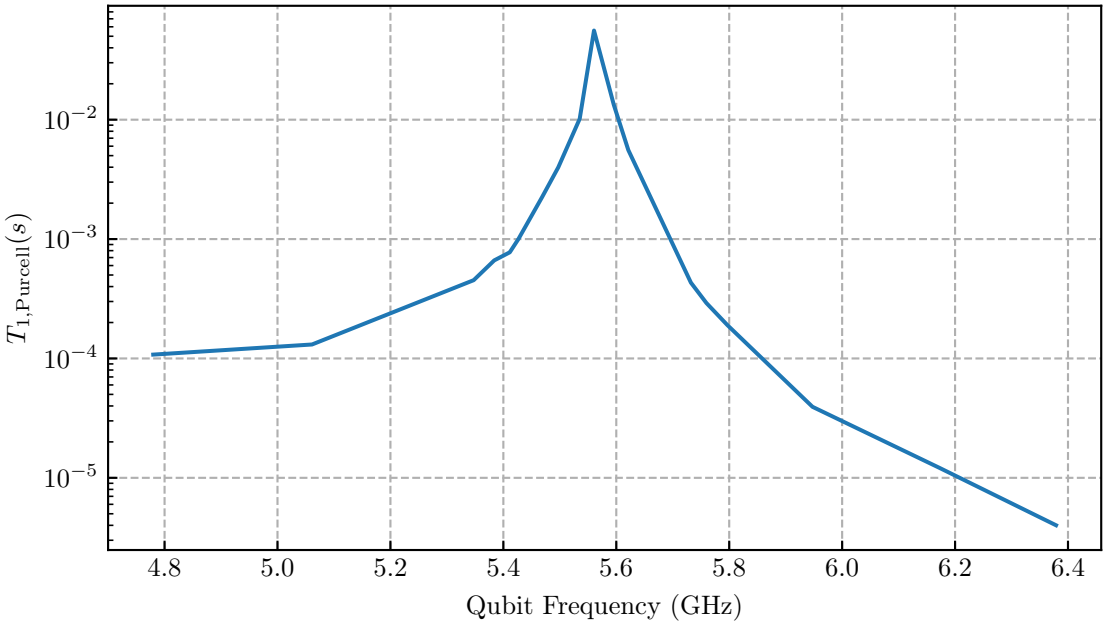

Figure 4-16: Electromagnetic simulation of $T_{1,\mathrm{Purcell}}$ versus f_q for physical layout.

The Purcell-limited qubit lifetime is found by

$$T_{1,\mathrm{Purcell}} = \frac{1}{\Gamma_p} = \frac{Q_q}{\omega_q} \tag{4.20}$$

where Q_q is the loaded quality factor of the qubit mode. The Purcell-limited qubit lifetime versus qubit frequency is shown in Fig. 4-16. The design achieves a $T_{1,\mathrm{Purcell}} >$ 1 ms for a bandwidth of about 300 MHz.

The scattering parameters of the design in Fig. 4-14 are simulated. For comparison, scattering parameters are found both with and without the $\lambda_r/4$ resonator (see Fig. 4-17). As expected, the coupling to the cavity introduces a resonance in the reflection and transmission spectrum. Future work will examine how we can remove this visible resonance and still observe a qubit-state-dependent phase shift.

At frequencies away from the resonant point, the strong capacitive and inductive distributed coupling between the coplanar waveguides introduces impedance mismatch [42]. This results in an increase in reflection and a slight decrease in transmission across the spectrum. This can be further improved with fine-tuning of the coplanar waveguide dimensions to better match the impedance at the coupling point

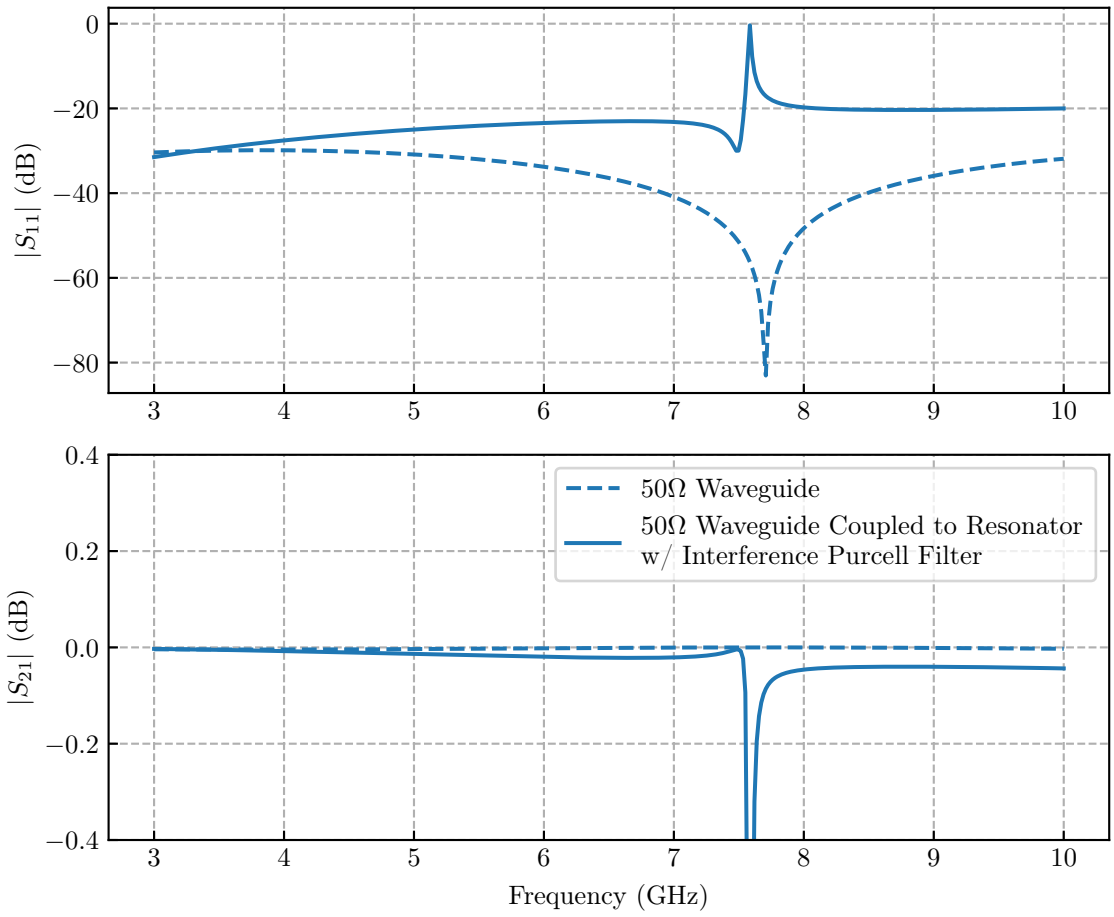

Figure 4-17: S-parameters to evaluate how well the impedance environment of the transmission line bus is preserved. The length of the 50 Ω waveguides is the same with and without coupling to a resonator. No weakly-coupled port is used.

between the readout bus and resonator's coplanar waveguides.

Chapter 5

Conclusion and Outlook

In this thesis, we have detailed the design of a hardware-efficient Purcell filter that couples the readout resonator to two points on the readout bus to create a destructive interference effect that protects the qubit from Purcell decay. This Purcell suppression holds for large resonator decays, making it a suitable design as quantum computers trend toward faster qubit readout.

This filter is a building block toward a more scalable and modular architecture for the readout of superconducting qubits. Rather than be used in conventional designs which interrupt the readout bus with an "open" or weakly-coupled port, the proposed interference Purcell filter would be used in a scheme that preserves the readout bus's $50\,\Omega$ environment, precluding the spatial dependence of readout resonator decay along the readout line and obviating the need for an impedance-matching circulator.

To achieve the same or better directionality of transmission measurement as that with a weakly-coupled port, we envision a form of readout that uses "directional" resonators. A conceptual diagram of this readout is shown in Fig. 3-3. This "directional" readout demonstrates promise to be more scalable and modular, with significant potential to expedite the design of many-qubit systems. The Purcell filter described in this thesis is the first of its kind to be compatible with this form of directional readout.

Bibliography

[1] A. Aspuru-Guzik, A. D. Dutoi, P. J. Love, and M. Head-Gordon. "Simulated Quantum Computation of Molecular Energies". In: *Science* 309.5741 (2005), pp. 1704–1707. ISSN: 0036-8075, 1095-9203. DOI: 10.1126/science.1113479.

[2] E. Farhi et al. "A Quantum Adiabatic Evolution Algorithm Applied to Random Instances of an NP-Complete Problem". In: *Science* 292.5516 (2001), pp. 472–475. DOI: 10.1126/science.1057726.

[3] P. W. Shor. "Polynomial-Time Algorithms for Prime Factorization and Discrete Logarithms on a Quantum Computer". In: *SIAM Journal on Computing* 26.5 (1997), pp. 1484–1509. ISSN: 0097-5397, 1095-7111. DOI: 10.1137/S0097539795293172.

[4] J. Biamonte et al. "Quantum Machine Learning". In: *Nature* 549.7671 (2017), pp. 195–202. ISSN: 1476-4687. DOI: 10.1038/nature23474.

[5] M. H. Devoret and R. J. Schoelkopf. "Superconducting Circuits for Quantum Information: An Outlook". In: *Science* 339.6124 (2013), pp. 1169–1174. ISSN: 0036-8075, 1095-9203. DOI: 10.1126/science.1231930.

[6] A. Blais, A. L. Grimsmo, S. M. Girvin, and A. Wallraff. "Circuit Quantum Electrodynamics". In: *Reviews of Modern Physics* 93.2 (2021), p. 025005. ISSN: 0034-6861, 1539-0756. DOI: 10.1103/RevModPhys.93.025005.

[7] R. Acharya et al. *Suppressing Quantum Errors by Scaling a Surface Code Logical Qubit*. 2022. DOI: 10.48550/arXiv.2207.06431.

[8] S. Krinner et al. "Realizing Repeated Quantum Error Correction in a Distance-Three Surface Code". In: *Nature* 605.7911 (2022), pp. 669–674. ISSN: 0028-0836, 1476-4687. DOI: 10.1038/s41586-022-04566-8.

[9] Z. Chen et al. "Exponential Suppression of Bit or Phase Errors with Cyclic Error Correction". In: *Nature* 595.7867 (2021), pp. 383–387. ISSN: 1476-4687. DOI: 10.1038/s41586-021-03588-y.

[10] A. Blais, R.-S. Huang, A. Wallraff, S. M. Girvin, and R. J. Schoelkopf. "Cavity Quantum Electrodynamics for Superconducting Electrical Circuits: An Architecture for Quantum Computation". In: *Physical Review A* 69.6 (2004), p. 062320. ISSN: 1050-2947, 1094-1622. DOI: 10.1103/PhysRevA.69.062320.

[11] D. I. Schuster et al. "Ac Stark Shift and Dephasing of a Superconducting Qubit Strongly Coupled to a Cavity Field". In: *Physical Review Letters* 94.12 (2005), p. 123602. ISSN: 0031-9007, 1079-7114. DOI: 10.1103/PhysRevLett.94.123602.

[12] C. M. Caves. "Quantum Limits on Noise in Linear Amplifiers". In: *Physical Review D* 26.8 (1982), pp. 1817–1839. DOI: 10.1103/PhysRevD.26.1817.

[13] B. Yurke, M. L. Roukes, R. Movshovich, and A. N. Pargellis. "A Low-noise Series-array Josephson Junction Parametric Amplifier". In: *Applied Physics Letters* 69.20 (1996), pp. 3078–3080. ISSN: 0003-6951. DOI: 10.1063/1.116845.

[14] M. A. Castellanos-Beltran, K. D. Irwin, G. C. Hilton, L. R. Vale, and K. W. Lehnert. "Amplification and Squeezing of Quantum Noise with a Tunable Josephson Metamaterial". In: *Nature Physics* 4.12 (2008), pp. 929–931. ISSN: 1745-2481. DOI: 10.1038/nphys1090.

[15] K. O'Brien, C. Macklin, I. Siddiqi, and X. Zhang. "Resonant Phase Matching of Josephson Junction Traveling Wave Parametric Amplifiers". In: *Physical Review Letters* 113.15 (2014), p. 157001. ISSN: 0031-9007, 1079-7114. DOI: 10.1103/PhysRevLett.113.157001.

[16] C. Macklin et al. "A Near-Quantum-Limited Josephson Traveling-Wave Parametric Amplifier". In: *Science* 350.6258 (2015), pp. 307–310. ISSN: 0036-8075, 1095-9203. DOI: 10.1126/science.aaa8525.

[17] E. Purcell. "Proceedings of the American Physical Society". In: *Physical Review* 69.11-12 (1946), pp. 674–674. ISSN: 0031-899X. DOI: 10.1103/PhysRev.69.674.

[18] E. Jeffrey et al. "Fast Accurate State Measurement with Superconducting Qubits". In: *Physical Review Letters* 112.19 (2014), p. 190504. DOI: 10.1103/PhysRevLett.112.190504.

[19] E. A. Sete, J. M. Martinis, and A. N. Korotkov. "Quantum Theory of a Bandpass Purcell Filter for Qubit Readout". In: *Physical Review A* 92.1 (2015), p. 012325. ISSN: 1050-2947, 1094-1622. DOI: 10.1103/PhysRevA.92.012325.

[20] J. Heinsoo et al. "Rapid High-fidelity Multiplexed Readout of Superconducting Qubits". In: *Physical Review Applied* 10.3 (2018), p. 034040. DOI: 10.1103/PhysRevApplied.10.034040.

[21] Y. Sunada et al. "Fast Readout and Reset of a Superconducting Qubit Coupled to a Resonator with an Intrinsic Purcell Filter". In: *Physical Review Applied* 17.4 (2022), p. 044016. ISSN: 2331-7019. DOI: 10.1103/PhysRevApplied.17.044016.

[22] S. M. Girvin. "Circuit QED: Superconducting Qubits Coupled to Microwave Photons". In: *Quantum Machines: Measurement and Control of Engineered Quantum Systems*. Ed. by M. Devoret, B. Huard, R. Schoelkopf, and L. F. Cugliandolo. Oxford University Press, 2014, pp. 113–256. ISBN: 978-0-19-968118-1. DOI: 10.1093/acprof:oso/9780199681181.003.0003.

[23] M. Tinkham. *Introduction to Superconductivity*. 2 ed. Dover Books on Physics. Mineola, NY: Dover Publ, 2015. 454 pp. ISBN: 978-0-486-43503-9.

[24] P. Krantz et al. "A Quantum Engineer's Guide to Superconducting Qubits". In: *Applied Physics Reviews* 6.2 (2019), p. 021318. ISSN: 1931-9401. DOI: 10.1063/1.5089550.

[25] J. Koch et al. "Charge-Insensitive Qubit Design Derived from the Cooper Pair Box". In: *Physical Review A* 76.4 (2007), p. 042319. ISSN: 1050-2947, 1094-1622. DOI: 10.1103/PhysRevA.76.042319.

[26] S. E. Nigg et al. "Black-Box Superconducting Circuit Quantization". In: *Physical Review Letters* 108.24 (2012), p. 240502. ISSN: 0031-9007, 1079-7114. DOI: 10.1103/PhysRevLett.108.240502.

[27] F. Solgun, D. P. DiVincenzo, and J. M. Gambetta. "Simple Impedance Response Formulas for the Dispersive Interaction Rates in the Effective Hamiltonians of Low Anharmonicity Superconducting Qubits". In: *IEEE Transactions on Microwave Theory and Techniques* 67.3 (2019), pp. 928–948. ISSN: 0018-9480, 1557-9670. DOI: 10.1109/TMTT.2019.2893639.

[28] A. Wallraff et al. "Strong Coupling of a Single Photon to a Superconducting Qubit Using Circuit Quantum Electrodynamics". In: *Nature* 431.7005 (2004), pp. 162–167. ISSN: 0028-0836, 1476-4687. DOI: 10.1038/nature02851.

[29] N. Didier, J. Bourassa, and A. Blais. "Fast Quantum Non-Demolition Readout from Longitudinal Qubit-Oscillator Interaction". In: *Physical Review Letters* 115.20 (2015), p. 203601. ISSN: 0031-9007, 1079-7114. DOI: 10.1103/PhysRevLett.115.203601.

[30] A. J. Kerman. "Quantum Information Processing Using Quasiclassical Electromagnetic Interactions between Qubits and Electrical Resonators". In: *New Journal of Physics* 15.12 (2013), p. 123011. ISSN: 1367-2630. DOI: 10.1088/1367-2630/15/12/123011.

[31] R. Dassonneville et al. "Fast High-Fidelity Quantum Nondemolition Qubit Readout via a Nonperturbative Cross-Kerr Coupling". In: *Physical Review X* 10.1 (2020), p. 011045. ISSN: 2160-3308. DOI: 10.1103/PhysRevX.10.011045.

[32] H. A. Haus. *Waves and Fields in Optoelectronics*. Prentice-Hall Series in Solid State Physical Electronics. Englewood Cliffs, NJ: Prentice-Hall, 1984. 402 pp. ISBN: 978-0-13-946053-1.

[33] A. A. Clerk, M. H. Devoret, S. M. Girvin, F. Marquardt, and R. J. Schoelkopf. "Introduction to Quantum Noise, Measurement and Amplification". In: *Reviews of Modern Physics* 82.2 (2010), pp. 1155–1208. ISSN: 0034-6861, 1539-0756. DOI: 10.1103/RevModPhys.82.1155.

[34] F. Yan et al. "The Flux Qubit Revisited to Enhance Coherence and Reproducibility". In: *Nature Communications* 7.1 (2016), p. 12964. ISSN: 2041-1723. DOI: 10.1038/ncomms12964.

[35] T. Walter et al. "Rapid High-Fidelity Single-Shot Dispersive Readout of Superconducting Qubits". In: *Physical Review Applied* 7.5 (2017), p. 054020. ISSN: 2331-7019. DOI: 10.1103/PhysRevApplied.7.054020.

[36] *IBM Quantum Hub to Spur Academic, Commercial Quantum Ecosystem*. IBM Research Blog. 2018. URL: https://www.ibm.com/blogs/research/2018/05/ibm-q-hub-asia/.

[37] N. Roch et al. "Observation of Measurement-Induced Entanglement and Quantum Trajectories of Remote Superconducting Qubits". In: *Physical Review Letters* 112.17 (2014), p. 170501. ISSN: 0031-9007, 1079-7114. DOI: 10.1103/PhysRevLett.112.170501.

[38] A. Kamal, J. Clarke, and M. H. Devoret. "Noiseless Non-Reciprocity in a Parametric Active Device". In: *Nature Physics* 7.4 (2011), pp. 311–315. ISSN: 1745-2481. DOI: 10.1038/nphys1893.

[39] B. J. Chapman et al. "Widely Tunable On-Chip Microwave Circulator for Superconducting Quantum Circuits". In: *Physical Review X* 7.4 (2017), p. 041043. DOI: 10.1103/PhysRevX.7.041043.

[40] B. J. Chapman, E. I. Rosenthal, and K. W. Lehnert. "Design of an On-Chip Superconducting Microwave Circulator with Octave Bandwidth". In: *Physical Review Applied* 11.4 (2019), p. 044048. DOI: 10.1103/PhysRevApplied.11.044048.

[41] A. G. Fowler, M. Mariantoni, J. M. Martinis, and A. N. Cleland. "Surface Codes: Towards Practical Large-Scale Quantum Computation". In: *Physical Review A* 86.3 (2012), p. 032324. ISSN: 1050-2947, 1094-1622. DOI: 10.1103/PhysRevA.86.032324.

[42] S. J. Orfanidis. *Electromagnetic Waves and Antennas*. 2016.

[43] M. F. Gely and G. A. Steele. "QuCAT: Quantum Circuit Analyzer Tool in Python". In: *New Journal of Physics* 22.1 (2020), p. 013025. ISSN: 1367-2630. DOI: 10.1088/1367-2630/ab60f6.

[44] D. Pozar. *Microwave Engineering*. 2012.

[45] M.-H. Mao, R.-B. Wu, C.-H. Chen, and C.-H. Lin. "Characterization of Coplanar Waveguide Open End Capacitance-Theory and Experiment". In: *IEEE Transactions on Microwave Theory and Techniques* 42.6 (1994), pp. 1016–1024. ISSN: 1557-9670. DOI: 10.1109/22.293571.

[46] Z. K. Minev et al. "Energy-Participation Quantization of Josephson Circuits". In: *npj Quantum Inf* 7.131 (2021). DOI: 10.1038/s41534-021-00461-8.